The Astrophysical Journal Letters, 960:L3 (24pp), 2024 January 1 https://doi.org/10.3847/2041-8213/ad1691
© 2024. The Author(s). Published by the American Astronomical Society.
OPEN ACCESS

New Mass and Radius Constraints on the LHS 1140 Planets: LHS 1140 b Is either a Temperate Mini-Neptune or a Water World

Charles Cadieux[1], Mykhaylo Plotnykov[2], René Doyon[1,3], Diana Valencia[4,5], Farbod Jahandar[1], Lisa Dang[1], Martin Turbet[6,7], Thomas J. Fauchez[8,9,10], Ryan Cloutier[11], Collin Cherubim[12,13], Étienne Artigau[1,3], Neil J. Cook[1], Billy Edwards[14,15], Tim Hallatt[1,16], Benjamin Charnay[17], François Bouchy[18], Romain Allart[1], Lucile Mignon[18], Frédérique Baron[1], Susana C. C. Barros[19,20], Björn Benneke[1], B. L. Canto Martins[21], Nicolas B. Cowan[16,22], J. R. De Medeiros[21], Xavier Delfosse[23], Elisa Delgado-Mena[19], Xavier Dumusque[18], David Ehrenreich[18], Yolanda G. C. Frensch[18], J. I. González Hernández[24,25], Nathan C. Hara[18], David Lafrenière[1], Gaspare Lo Curto[26], Lison Malo[1,3], Claudio Melo[26], Dany Mounzer[18], Vera Maria Passeger[24,25,27], Francesco Pepe[18], Anne-Sophie Poulin-Girard[28], Nuno C. Santos[19,20], Danuta Sosnowska[18], Alejandro Suárez Mascareño[24,25], Simon Thibault[29], Valentina Vaulato[18], Gregg A. Wade[30], and François Wildi[18]

[1] Institut Trottier de recherche sur les exoplanètes, Université de Montréal, 1375 Ave Thérèse-Lavoie-Roux, Montréal, QC H2V 0B3, Canada; charles.cadieux.1@umontreal.ca
[2] Department of Physics, University of Toronto, Toronto, ON M5S 3H4, Canada
[3] Observatoire du Mont-Mégantic, Université de Montréal, Montréal, QC H3C 3J7, Canada
[4] Department of Physical & Environmental Sciences, University of Toronto at Scarborough, Toronto, ON M1C 1A4, Canada
[5] David A. Dunlap Department of Astronomy & Astrophysics, University of Toronto, 50 St. George Street, Toronto, ON M5S 3H4, Canada
[6] Laboratoire de Météorologie Dynamique/IPSL, CNRS, Sorbonne Université, Ecole Normale Supérieure, PSL Research University, Ecole Polytechnique, F-75005 Paris, France
[7] Laboratoire d'astrophysique de Bordeaux, Univ. Bordeaux, CNRS, B18N, allée Geoffroy Saint-Hilaire, F-33615 Pessac, France
[8] NASA Goddard Space Flight Center, 8800 Greenbelt Road, Greenbelt, MD 20771, USA
[9] Integrated Space Science and Technology Institute, Department of Physics, American University, Washington, DC, USA
[10] NASA GSFC Sellers Exoplanet Environments Collaboration, 8800 Greenbelt Road, Greenbelt, MD 20771, USA
[11] Department of Physics & Astronomy, McMaster University, 1280 Main Street West, Hamilton, ON L8S 4L8, Canada
[12] Earth and Planetary Science, Harvard University, 20 Oxford Street, Cambridge, MA 02138, USA
[13] Center for Astrophysics | Harvard & Smithsonian, 60 Garden Street, Cambridge, MA 02138, USA
[14] SRON, Netherlands Institute for Space Research, Niels Bohrweg 4, NL-2333 CA, Leiden, The Netherlands
[15] Department of Physics and Astronomy, University College London, London, UK
[16] Department of Physics and Trottier Space Institute, McGill University, Montréal, QC H3A 2T8, Canada
[17] LESIA, Observatoire de Paris, Université PSL, CNRS, Sorbonne Université, Université Paris-Cité, 5 place Jules Janssen, F-92195 Meudon, France
[18] Departement d'astronomie, Université de Genève, Chemin Pegasi, 51, CH-1290 Versoix, Switzerland
[19] Instituto de Astrofísica e Ciências do Espaço, Universidade do Porto, CAUP, Rua das Estrelas, PT4150-762 Porto, Portugal
[20] Departamento de Fisica e Astronomia, Faculdade de Ciencias, Universidade do Porto, Rua Campo Alegre, 4169-007 Porto, Portugal
[21] Departamento de Física Teórica e Experimental, Universidade Federal do Rio Grande do Norte, Campus Universitário, Natal, RN, 59072-970, Brazil
[22] Department of Earth & Planetary Sciences, McGill University, 3450 rue University, Montréal, QC H3A 0E8, Canada
[23] Univ. Grenoble Alpes, CNRS, IPAG, F-38000 Grenoble, France
[24] Instituto de Astrofísica de Canarias, E-38205 La Laguna, Tenerife, Spain
[25] Departamento de Astrofísica, Universidad de La Laguna, E-38206 La Laguna, Tenerife, Spain
[26] European Southern Observatory, Karl-Schwarzschild-Strasse 2, D-85748 Garching, Germany
[27] Hamburger Sternwarte, Gojenbergsweg 112, D-21029 Hamburg, Germany
[28] ABB, Québec, G1P 0B2, Canada
[29] Centre d'optique, photonique et lasers, Université Laval, Québec, G1V 0A6, Canada
[30] Department of Physics and Space Science, Royal Military College of Canada, P.O. Box 17000, Station Forces, Kingston, ON, Canada
Received 2023 October 23; revised 2023 December 9; accepted 2023 December 15; published 2024 January 3

Abstract

The two-planet transiting system LHS 1140 has been extensively observed since its discovery in 2017, notably with Spitzer, HST, TESS, and ESPRESSO, placing strong constraints on the parameters of the M4.5 host star and its small temperate exoplanets, LHS 1140 b and c. Here, we reanalyze the ESPRESSO observations of LHS 1140 with the novel line-by-line framework designed to fully exploit the radial velocity content of a stellar spectrum while being resilient to outlier measurements. The improved radial velocities, combined with updated stellar parameters, consolidate our knowledge of the mass of LHS 1140 b ($5.60 \pm 0.19\,M_{\oplus}$) and LHS 1140 c ($1.91 \pm 0.06\,M_{\oplus}$) with an unprecedented precision of 3%. Transits from Spitzer, HST, and TESS are jointly analyzed for the first time, allowing us to refine the planetary radii of b ($1.730 \pm 0.025\,R_{\oplus}$) and c ($1.272 \pm 0.026\,R_{\oplus}$). Stellar abundance measurements of refractory elements (Fe, Mg, and Si) obtained with NIRPS are used to constrain the internal structure of LHS 1140 b. This planet is unlikely to be a rocky super-Earth, as previously reported, but rather a mini-Neptune with a ~0.1% H/He envelope by mass or a water world with a water-mass fraction between 9% and 19%, depending on the atmospheric composition and relative abundance of Fe and Mg. While the mini-Neptune case would not be habitable, a water-abundant LHS 1140 b potentially has

Original content from this work may be used under the terms of the Creative Commons Attribution 4.0 licence. Any further distribution of this work must maintain attribution to the author(s) and the title of the work, journal citation and DOI.

habitable surface conditions according to 3D global climate models, suggesting liquid water at the substellar point for atmospheres with relatively low CO_2 concentration, from Earth-like to a few bars.

Unified Astronomy Thesaurus concepts: Exoplanets (498); Habitable planets (695); Super Earths (1655); M dwarf stars (982); Planetary interior (1248)

Supporting material: machine-readable table

1. Introduction

The last few years have been fruitful in the quest to uncover exoplanets transiting nearby low-mass stars. Unlike their solar counterparts, M dwarfs represent optimal targets for detailed studies of their planetary systems. They have smaller sizes (0.1–0.6 $R_\odot$) and masses (0.1–0.6 $M_\odot$), facilitating the characterization of exoplanets through transit and radial velocity (RV) observations. As they are less luminous, their habitable zone (HZ) is more compact than in our solar system, corresponding to orbital periods usually well sampled by current surveys (typically 60 days for an M0, 3 days for an M9). M dwarfs have at least twice as many small exoplanets with $M_p \sin i < 10\ M_\oplus$ than G-type stars (Sabotta et al. 2021) and make up the majority of systems in the vicinity of the Sun (Reylé et al. 2021, 2022). We thus expect the nearest HZ planets to orbit such stars. This is exemplified with Proxima Centauri (M5.5V), our closest neighbor (1.3 pc; Gaia Collaboration et al. 2021), hosting a nontransiting terrestrial planet in the HZ (Anglada-Escudé et al. 2016; Faria et al. 2022). The M5.5V dwarf GJ 1002 at 4.84 pc also has two nontransiting Earth-mass companions in the HZ recently discovered by Suárez Mascareño et al. (2023). The TRAPPIST-1 system (Gillon et al. 2017) at 12.5 pc has seven terrestrial planets, including three in the HZ, all transiting the M8V ultracool host. These transiting systems are extremely valuable because the radius of exoplanets—sometimes even the mass through transit timing variations as for TRAPPIST-1 (e.g., Agol et al. 2021)—is only accessible via the transit method. Combined with dynamical mass constraints from Doppler spectroscopy, the bulk density of exoplanets can be obtained, revealing whether their interior is mostly rocky, gaseous, or perhaps even water-rich (Luque & Pallé 2022), but evidence of water worlds remains elusive (Rogers et al. 2023).

The M4.5 dwarf LHS 1140 located at 15.0 pc is another intriguing system, currently the second-closest to a transiting HZ exoplanet after TRAPPIST-1. A super-Earth on a 24.7 day temperate orbit was detected in 2017 (Dittmann et al. 2017, hereafter D17) from MEarth photometry (Irwin et al. 2009), followed by the discovery of a second rocky planet with a shorter 3.8 day period (Ment et al. 2019, hereafter M19). The follow-up study of M19 presents a transit visit of LHS 1140 b and c with the Spitzer Space Telescope, largely improving the radius constraints of the two planets. Their masses were derived from HARPS (Pepe et al. 2002) RVs, initially for b only by D17 and subsequently for b and c by M19 using an extended data set. This planetary system was revisited in 2020 (Lillo-Box et al. 2020, hereafter LB20) with the ESPRESSO spectrograph (Pepe et al. 2021) and the Transiting Exoplanet Survey Satellite (TESS; Ricker et al. 2015), offering an update of the bulk densities of LHS 1140 b and c while also hinting at a possible third nontransiting planet on a longer orbit ($P_d = 78.9$ days). Lastly, transit spectroscopy of LHS 1140 b has been obtained from the ground (Diamond-Lowe et al. 2020) and from space (Edwards et al. 2021) with the Wide Field Camera 3 (WFC3) on the Hubble Space Telescope (HST). Edwards et al. (2021) reported a tentative detection of a hydrogen-dominated atmosphere with H_2O on LHS 1140 b, but the signal (∼100 ppm) could also be explained by stellar contamination.

In this letter, we present a new analysis of archival data of LHS 1140 and derive stellar abundances from near-infrared spectroscopy with the Near-InfraRed Planet Searcher (NIRPS; Bouchy et al. 2017). The ESPRESSO RVs were significantly improved using a line-by-line (LBL) extraction (Artigau et al. 2022), and, for the first time, transit data sets from Spitzer, HST, and TESS were jointly analyzed. We describe the observations in Section 2 and characterize the host star in Section 3. We present our revision of the mass and radius of the LHS 1140 planets and discuss their plausible internal structures in Section 4. Concluding remarks follow in Section 5.

2. Observations

2.1. Spitzer Photometry

We recovered four Spitzer transits of LHS 1140 b taken with the Infrared Array Camera (Fazio et al. 2004) at 4.5 μm from the NASA/IPAC Infrared Science Archive.[31] These data include the double transit of LHS 1140 b and c analyzed by M19, with three additional unpublished transits of LHS 1140 b (PI: J. A. Dittmann) from the same program. The observations were taken on UT 2017 October 2, 2017 October 27, 2018 March 24, and 2018 April 18, hereafter referred to as transits 1–4 (transit 4 is presented in M19).

The observations were acquired using the subarray mode with a 2 s exposure producing data cubes of 64 subarray images of 32×32 pixels. We used the Spitzer Phase Curve Analysis pipeline (Dang et al. 2018; Bell et al. 2021) to extract the photometry and decorrelate against instrumental systematics. For transits 1 and 3, we use a 3×3 pixel area to extract the target's intensity for each subarray frame. We then median-binned each data cube to mitigate the known subarray instrumental systematics and used pixel level decorrelation (PLD; Deming et al. 2015) to detrend against detector systematics. Similarly to M19, we elected to discard the first 78 minutes of transit 4, during which the target's centroid had not yet settled on the detector. For transits 2 and 4, we opted for a different detrending strategy, as the shorter baseline before transit tends to bias the retrieved eclipse depth with PLD. Instead, we find that extracting the target photometry with an exact circular aperture with a radius of 3.0 pixels centered on the target's centroid yields the optimal photometric scheme. We then binned each data cube and detrended the instrumental systematics using a 2D polynomial as a function of the centroid. The stacked (phase-folded) transit of LHS 1140 b is presented in Figure 1. The individual detrended transits are presented Figure A1.

[31] irsa.ipac.caltech.edu/

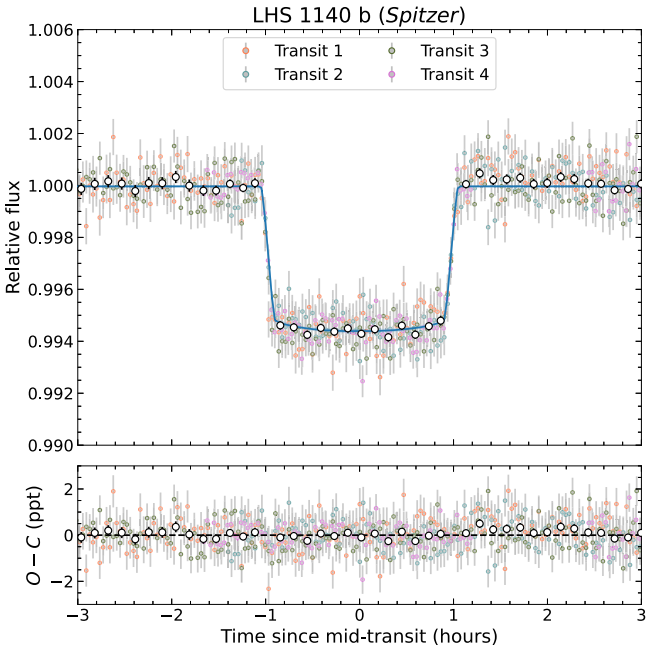

Figure 1. Phase-folded transit of LHS 1140 b observed with the Spitzer Infrared Array Camera (at 4.5 μm). The transit of LHS 1140 c from transit 4 is masked (see Figure A1 for individual transits). The open circles represent 8 minute binned photometry, and the blue curve depicts the best-fit transit model. The residuals of this fit are shown below.

2.2. HST WFC3 White Light Curve

Two transits of LHS 1140 b were observed with HST WFC3 on UT 2017 January 28 and UT 2017 December 15 (PN: 14888; PI: J. A. Dittmann). Unfortunately, due to large shifts in the position of the spectrum on the detector, the observation from UT 2017 January 28 could not be reliably analyzed (Edwards et al. 2021). The transit on UT 2017 December 15 was successfully analyzed by Edwards et al. (2021) to constrain the transmission spectrum of LHS 1140 b near 1.4 μm. The observations were conducted in the G141 grism configuration with the GRISM256 aperture (256×256 subarray) and 103.13 s integration time. Readers are referred to Edwards et al. (2021) for a complete description of the HST data reduction that made use of the Iraclis software (Tsiaras et al. 2016). Here, we include the extracted white light curve from HST (Figure A2) for our transit analysis.

2.3. TESS Photometry

LHS 1140 (TIC 92226327, TOI-256) was observed with TESS at a 2 minute cadence during its primary mission from 2018 September 20 to October 17 (sector 3) and during its first extended mission from 2020 September 23 to October 20 (sector 30). We used the Presearch Data Conditioning Simple Aperture Photometry (PDCSAP; Smith et al. 2012; Stumpe et al. 2012, 2014) data product issued by the TESS Science Processing Operations Center (SPOC; Jenkins et al. 2016) at NASA Ames Research Center and available on the Mikulski Archive for Space Telescopes.[32] The PDCSAP data include corrections for instrumental systematics and for flux dilution from known Gaia sources within several TESS pixels ($21''$ pixel^{-1}). The light curve from sector 3 was reprocessed with a more recent release of SPOC (version 5.0.20), which applies the new background correction implemented for the extended mission to the first sectors of TESS. This new correction typically reduces the inferred transit depths by less than 2%. Using the same pipeline (SPOC v5.0) for sectors 3 and 30 ensures consistent transit depths for LHS 1140 b and c between primary and extended mission data. The full TESS light curve of LHS 1140 shown in Figure A3 captures 2 and 11 transits of planets b and c, respectively, twice as many as in LB20 based on sector 3 data only. The phase-folded transits from TESS are also shown in Figure A3.

2.4. ESPRESSO RV

We retrieved publicly available ESPRESSO data of LHS 1140 from the European Southern Observatory (ESO) science archive[33] (Delmotte et al. 2006). These data consist of the same 117 spectra analyzed in LB20 and taken with the SINGLEHR21 mode between 2018 October and 2019 December. We used the bias- and dark-subtracted, extracted, and flat-fielded spectra reduced with the ESPRESSO pipeline (version 2.2.1).[34] The RV extraction from the reduced data was performed with the LBL (version 0.52) method of Artigau et al. (2022), available as an open-source package.[35] A simple telluric correction is first performed inside the LBL code by fitting a TAPAS (Bertaux et al. 2014) atmospheric model. This correction step, comparable to the approach of Allart et al. (2022), has been demonstrated to improve the RV precision of ESPRESSO, particularly for M-type stars.

At the core of the LBL method, first explored by Dumusque (2018), Doppler shifts are measured on the smallest spectral range possible, i.e., a spectral line, from a high signal-to-noise ratio (S/N) template spectrum of the star and its first derivative (Bouchy et al. 2001). This template is constructed by coadding all of our 117 telluric-corrected spectra. Then, the statistical consistency between all per-line velocities (~38,000 for LHS 1140) is verified using a simple mixture model (Appendix B of Artigau et al. 2022) that effectively removes high-sigma outliers to produce a final error-weighted average of valid lines. This approach fully exploits the RV content of a stellar spectrum and is conceptually similar to widely employed template-matching algorithms (e.g., Anglada-Escudé & Butler 2012; Astudillo-Defru et al. 2017; Zechmeister et al. 2018; Silva et al. 2022) while being more resilient to outlying spectral features (e.g., telluric residuals, cosmic rays, and detector defects).

Following LB20, we separately analyzed the data taken before and after the fiber link change of ESPRESSO in 2019 June (Pepe et al. 2021), hereafter designated as "pre" and "post" velocities. Using an iterative sigma-clipping algorithm, we removed two epochs (BJD = 2458703.787210 and 2458766.704332) flagged as $>3\sigma$ outliers. The final RVs are given in Table B1 and show a median uncertainty of 0.36 m s^{-1} and dispersion (rms) of 4.07 m s^{-1}. As a comparison, the published values of LB20 derived from the cross-correlation function (CCF) technique have a median precision of 0.99 m s^{-1}, almost three times larger than LBL, and a 4.76 m s^{-1} scatter. Figure 2 presents a comparison between LBL and CCF for the best-fit orbits of LHS 1140 b and c. The

[32] archive.stsci.edu/tess/

[33] archive.eso.org/

[34] eso.org/sci/software/pipelines/espresso/

[35] github.com/njcuk9999/lbl

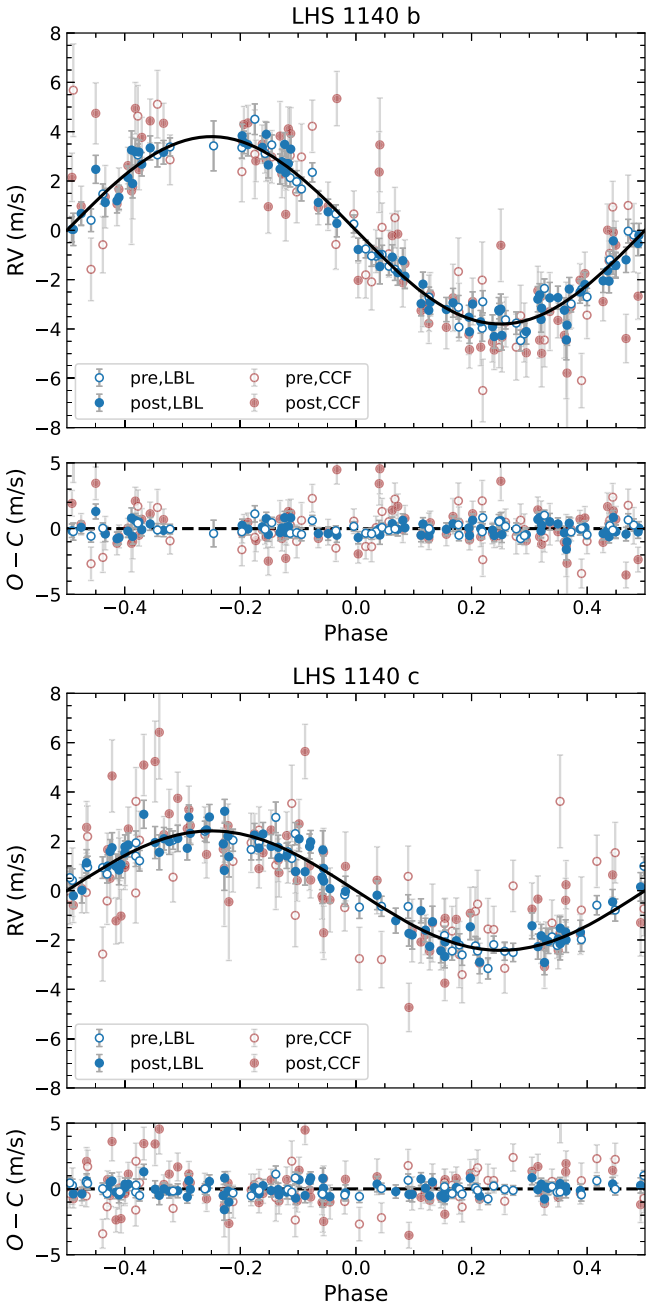

Figure 2. Phase-folded Keplerian signals of LHS 1140 b (top) and c (bottom) with ESPRESSO from RVs produced with the LBL method in blue and CCF in red (LB20). Open and filled data points represent pre- and post-fiber upgrade of ESPRESSO (2019 June). The best-fit circular orbital solutions (black curves) of LHS 1140 b ($K_b = 3.80 \pm 0.11$ m s^{-1}) and c ($K_c = 2.42 \pm 0.07$ m s^{-1}) are respectively improved by 50% and 70% compared with previous estimates with CCF. The residual rms is equivalent to 0.50 m s^{-1} for LBL and 1.28 m s^{-1} for CCF.

full LBL RV sequence is shown in Figure B1. Given the extreme precision of ESPRESSO with LBL, a joint analysis with the HARPS data also available through the ESO archive has resulted in identical semiamplitudes for LHS 1140 b and c. For this reason and to simplify the analysis, we opted to only use ESPRESSO in this work. The ESPRESSO observations span approximately 400 days, a long enough baseline to characterize signals at longer periods, such as the candidate LHS 1140 d ($P_d = 78.9$ days) or the rotation of the star ($P_{rot} = 131$ days; D17). As discussed in Appendices D.1 and D.3, we find no evidence for LHS 1140 d and attribute this 80 day signal most likely to stellar activity.

2.5. NIRPS High-resolution Spectroscopy

We acquired 29 high-resolution spectra of LHS 1140 with NIRPS (Bouchy et al. 2017; Wildi et al. 2022) during one of its commissioning phases (Prog-ID 60.A-9109) from 2022 November 26 to 2022 December 6. NIRPS is a new echelle spectrograph designed for precision RV at the ESO 3.6 m telescope in La Silla, Chile, covering the *YJH* bands (980–1800 nm). The instrument is equipped with a high-order adaptive optics system and two observing modes, High Accuracy ($R \approx 85{,}000$, 0.″4 fiber) and High Efficiency (HE; $R \approx 70{,}000$, 0.″9 fiber), that can both be utilized simultaneously with HARPS. LHS 1140 was observed in HE mode as an RV standard star to test the stability of the instrument preceding the official start of NIRPS operation in 2023 April. The observations were reduced with `APERO` v0.7.271 (Cook et al. 2022), the standard data reduction software for the SPIRou near-infrared spectrograph (Donati et al. 2020), fully compatible with NIRPS. We built a template spectrum of LHS 1140 from the telluric-corrected data product from `APERO` to derive independent stellar parameters and the abundances of several elements (Section 3.2). This template spectrum combines 29 individual spectra, each with an S/N per pixel of about 70 in the middle of the *H* band.

3. Stellar Characterization

The star LHS 1140 was characterized in previous studies (D17; M19; LB20). In this section, we summarize our work to revise the stellar mass and radius and measure the effective temperature and stellar abundances with NIRPS. An analysis of the stellar kinematics confirming the age (>5 Gyr; D17) and galactic thin disk membership of LHS 1140 is presented in Appendix C.1.

3.1. Stellar Mass and Radius Update

We pulled the K_s magnitude (8.82 ± 0.02) of LHS 1140 from the Two Micron All Sky Survey (Skrutskie et al. 2006) and its distance d from Gaia DR3 (14.96 ± 0.01 pc; Gaia Collaboration et al. 2021). Then, from the absolute K_s magnitude (M_{K_s}) to $M_\star$ empirical relation of Mann et al. (2019), we obtain a stellar mass of $0.1844 \pm 0.0046\, M_\odot$, with uncertainty propagating the errors on K_s, d, and the scatter of this relation. This revised and more precise stellar mass is consistent with that of M19 ($M_\star = 0.179 \pm 0.014\, M_\odot$) obtained from a similar mass–luminosity calibration (Benedict et al. 2016) but using a smaller sample of nearby binaries. In a similar way but using the M_{K_s}–$R_\star$ relationship of Mann et al. (2015), we obtain a radius of $0.2153 \pm 0.0065\, R_\odot$ for LHS 1140. M19 determine the stellar radius from an analysis of the transits, yielding a slightly more precise $R_\star = 0.2139 \pm 0.0041\ R_\odot$. To make sure that our results are completely independent of previous analyses, we first adopt the value derived from Mann et al. (2015) as a prior, then further constrain the radius from the stellar density inferred from transits. This Bayesian method is detailed in Appendix C.2 and results in a new stellar mass and radius of $M_\star = 0.1844 \pm 0.0045\ M_\odot$ and $R_\star = 0.2159 \pm 0.0030\ R_\odot$. The stellar parameters of LHS 1140 are listed in Table C1.

3.2. Stellar Abundances from NIRPS

We follow the methodology of Jahandar et al. (2023), also applied in Cadieux et al. (2022) for TOI-1452 (M4) and Gan et al. (2023) for TOI-4201 (M0.5), to derive the effective temperature and the abundances of several chemical species in LHS 1140 from the NIRPS template spectrum. A global fit (χ^2 minimization) to a selection of strong spectral lines using ACES stellar models (Allard et al. 2012; Husser et al. 2013) convolved to match the NIRPS resolution resulted in $T_{\rm eff} = 3096 \pm 48$ K and [M/H] $= 0.01 \pm 0.04$ for LHS 1140. Note that we fixed $\log g = 5$ (cgs) for our grid of models in accordance with LHS 1140 (Table C1). This method was empirically calibrated for a $\log g$ of 5.0 ± 0.2 dex (Jahandar et al. 2023).

We then performed a series of fits for a fixed $T_{\rm eff} = 3100$ K on individual spectral lines of known chemical species to derive their elemental abundances (again following Jahandar et al. 2023). We show an example of this method in Figure C2 for the Al I line at 1675.514 nm from which we measure [Al/H] $= 0.0 \pm 0.1$ dex from this single line. The average abundances for all chemical species detected in LHS 1140 are given in Table C2, including the refractory elements Fe, Mg, and Si that form the bulk material of planetary cores and mantles. As shown in Table C3, LHS 1140 features a relatively low Fe/Mg weight ratio ($1.03^{+0.40}_{-0.29}$) compared to the Sun (1.87 $\pm$ 0.22) and other solar neighborhood M dwarfs, with a C/O measurement consistent with the solar value. The measured Fe/Mg abundance ratio is used later as input to planetary internal structure models (Section 4.2).

4. Results and Discussion

4.1. New Density Measurements

We measure the physical and orbital parameters of LHS 1140 b and c by jointly fitting transit and Keplerian models to the photometric (Spitzer, HST, and TESS) and RV (ESPRESSO) observations. The details of this joint transit RV fit are presented in Appendix D.1. Notably, the best-fit solution is two planets on circular orbits (Table D1) with no evidence of candidate LHS 1140 d. We adopt the average radius measured by Spitzer and TESS for LHS 1140 c but discuss an important discrepancy between the two measurements in Appendix D.2.

We infer a mass of $5.60 \pm 0.19\,M_\oplus$ for LHS 1140 b and $1.91 \pm 0.06\,M_\oplus$ for LHS 1140 c, as well as planetary radii of $1.730 \pm 0.025\,R_\oplus$ for b and $1.272 \pm 0.026\,R_\oplus$ for c. The LHS 1140 planets are among the best-characterized exoplanets to date, with relative uncertainties of only 3% for the mass and 2% for the radius, reaching a similar precision to the TRAPPIST-1 planets (Agol et al. 2021). These measurements correspond to bulk densities of 5.9 ± 0.3 and 5.1 ± 0.4 g cm^{-3} for planets b and c, respectively. The results of previous studies for the semiamplitudes (K) and scaled radii ($R_p/R_\star$) of the planets are shown in Table 1. Since LB20, our updated $R_p/R_\star$ ratios have increased back to M19 values. This change results from incorporating additional transits with Spitzer and HST, as we retrieve the same $R_p/R_\star$ as LB20 to 1σ when fitting the TESS data only (see Figure D1). Note that our revision of the mass and radius of LHS 1140 b and c is dominated (by more than 80%) by K and $R_p/R_\star$ changes, not by the update of stellar parameters.

We compare our updated mass and radius to the M dwarf exoplanet population in Figure 3 with various pure composition curves included in the same figure. A detailed analysis of the internal structure of LHS 1140 b is presented in Section 4.2. First examining LHS 1140 b in Figure 3, we see that our revised mass and radius are off the Earth-like track, contradicting previous results from M19 and LB20 that this planet is a rocky, larger version of Earth (super-Earth). The mode of the distribution lies above the pure Mg–Si rock sequence, a region of the mass–radius diagram requiring an additional input of light elements, i.e., gas (H_2, He) or ices (e.g., H_2O, CH_4, NH_3), to explain the observed radius. LHS 1140 b is on the lower limit of the synthetic sub-Neptune population around M dwarfs of Rogers et al. (2023; orange region in Figure 3) that has undergone thermal evolution and atmospheric mass loss (photoevaporation) over 5 Gyr assuming an initial H/He mass fraction between 0.1% and 30%. With a small $T_{\rm eq}$ of 226 K, Rogers et al. (2023) predict a $\sim$0.1% H/He mass fraction for LHS 1140 b, which we confirm through simulation in Section 4.2.1. Alternatively, the planet could be purely rocky or with a water-mass fraction (WMF) of 10%–20%, clearly not as high as the water-rich (50% H_2O) population suggested by Luque & Pallé (2022). Note that this latter scenario would involve a different formation mechanism, as suggested by recent studies (Cloutier & Menou 2020; Luque & Pallé 2022; Cherubim et al. 2023; Piaulet et al. 2023), where small planets around M dwarfs could directly accrete icy materials outside the water snow line before migrating inward, in which case sub-Neptunes would actually be water worlds rather than H/He-enveloped planets.

For LHS 1140 c, our mass measurement agrees with previous studies, but we show in Appendix D.2 that the Spitzer and TESS radii are in 4σ disagreement, complicating the determination of its internal structure. In Figure 3, we present the average Spitzer+TESS radius of LHS 1140 c most compatible with a rocky interior depleted in iron relative to Earth, but should the planet be smaller, as measured by TESS, an Earth-like interior remains plausible. However, given the planet size and higher $T_{\rm eq}$ of 422 K, a hydrogen-dominated atmosphere or an important water content ($\gtrsim$10% by mass) similar to LHS 1140 b are formally rejected.

Table 1
Comparison of the Semiamplitudes and Scaled Radii of the LHS 1140 Planets from Different Studies

Parameter	D17	M19	LB20	This Work
LHS 1140 b				
K (m s^{-1})	5.34 ± 1.10	4.85 ± 0.55	4.21 ± 0.24	3.80 ± 0.11
$R_p/R_\star$ (%)	7.08 ± 0.13	7.39 ± 0.01	7.02 ± 0.19	7.33 ± 0.04
LHS 1140 c				
K (m s^{-1})	...	2.35 ± 0.49	2.22 ± 0.20	2.42 ± 0.07
$R_p/R_\star$ (%)	...	5.49 ± 0.01	5.02 ± 0.16	5.39 ± 0.08

Note. D17 with MEarth and HARPS. M19 with MEarth (extended), Spitzer, and HARPS (extended). LB20 with TESS, HARPS (M19), and ESPRESSO. This work with Spitzer (extended), HST, TESS (extended), and ESPRESSO (LB20).

4.2. Nature of LHS 1140 b

The unprecedented precision of both the mass and radius of the LHS 1140 planets combined with stellar abundance measurements provide a unique opportunity to better constrain the nature of these planets. Because of the radius uncertainty

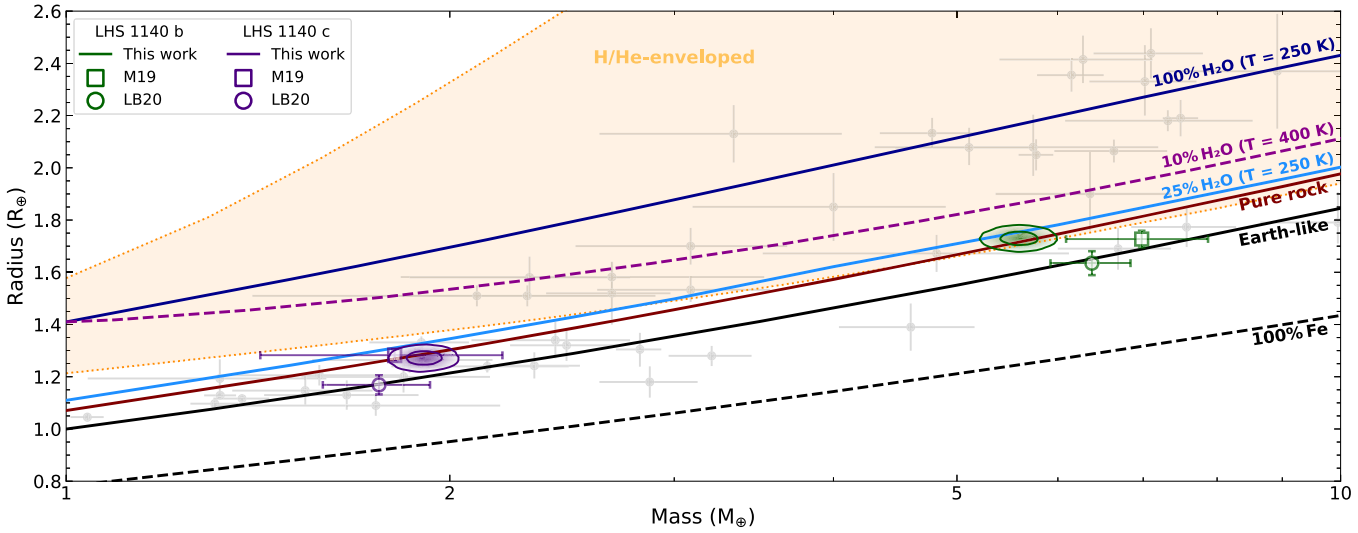

Figure 3. Mass–radius diagram of transiting exoplanets around M dwarfs (gray points) with well-established mass and radius (relative uncertainty <30%) from the NASA Exoplanet Archive (Akeson et al. 2013). Various theoretical composition curves from Guillot & Morel (1995), Valencia et al. (2007, 2013), and Aguichine et al. (2021) are plotted with the water-rich models assuming an Earth-like interior (33% iron by mass). The synthetic population of terrestrials enveloped in H/He (0.1%–30% initial mass fraction) of Rogers et al. (2023) is highlighted in orange. This region also highlights interior model degeneracy where the nature (H/He- or water-rich) of sub-Neptunes cannot be reliably determined from mass and radius alone. The mass and radius posteriors (1σ and 2σ contours) of LHS 1140 b (green) and LHS 1140 c (purple) from our joint transit RV analysis are drawn. Published values from LB20 derived from HARPS+ESPRESSO and TESS (sector 3) are shown with open circles. The results of M19 from HARPS and MEarth+Spitzer are presented with open squares.

associated with LHS 1140 c discussed above, we focus our analysis on LHS 1140 b. The mass–radius diagram of Figure 3 suggests three potential scenarios: (1) a mini-Neptune depleted in hydrogen, (2) a pure rocky (and airless) planet, and (3) a water world. All three possibilities are discussed below.

To address scenarios 2 and 3, we follow the method of Plotnykov & Valencia (2020), also applied to the water-world candidate TOI-1452 b (Cadieux et al. 2022), to constrain both the core-mass fraction (CMF) and water-mass fraction (WMF) of the planet. The adaptation of this method to LHS 1140 b is further detailed in Appendix E.1, with the posterior distributions available in Appendix E.2. In brief, this interior analysis treats the Fe/Mg ratio either as a free output parameter completely constrained by the mass–radius data (the no prior case) or as direct input informed by the measured stellar value (the stellar prior case) with $\mathrm{Fe/Mg_{planet}} \sim \mathcal{N}(\mathrm{Fe/Mg_{star}}, \sigma^2_{\mathrm{star}})$. This latter case assumes that stellar abundances are a good proxy of planetary abundances as suggested by planet formation studies (e.g., Bond et al. 2010; Thiabaud et al. 2015; Unterborn et al. 2016) and empirically (e.g., Dorn et al. 2017; Bonsor et al. 2021), though this correlation is not necessarily 1:1 (Adibekyan et al. 2021).

4.2.1. Hydrogen-poor Mini-Neptune

An Earth-like interior (CMF = 33%, WMF ∼ 0) overlaid by a solar mixture of hydrogen–helium contributing ∼0.1% of the mass and ∼10% of the radius could explain the density of LHS 1140 b. Here, we simulate the photoevaporation history of LHS 1140 b for 10 Gyr using the method of Cherubim et al. (2023) to verify whether such a hydrogen-rich envelope could survive at the present day. These simulations take into account thermal evolution and photoevaporation (e.g., Owen & Wu 2017) from stellar extreme-ultraviolet (EUV; 10–130 nm) and core-powered atmospheric escape (e.g., Ginzburg et al. 2018).

The results for a range of initial envelope mass fractions ($f_{\mathrm{atm},0}$ between 0.1% and 12%) are shown in Figure 4. Assuming that

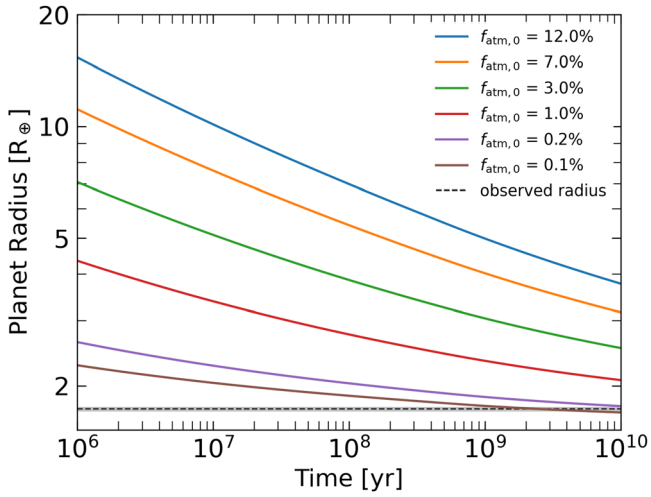

Figure 4. Primordial H/He atmosphere photoevaporation simulation of LHS 1140 b. Each curve corresponds to different initial envelope mass fractions $f_{\mathrm{atm},0}$. These simulations model thermal contraction, EUV-driven atmospheric escape, and core-powered mass loss using the methodology of Cherubim et al. (2023). $f_{\mathrm{atm},0} = 0.1\%$–$0.2\%$ is consistent with the observed radius given the age of the system (>5 Gyr).

LHS 1140 b did not undergo important migration after formation, it appears that $f_{\mathrm{atm},0} = 0.1\%$–$0.2\%$ (brown and purple curves in Figure 4) is in agreement with the observed radius after 5 Gyr, the minimum age estimate of the system. Since gas accretion models typically predict initial envelopes with mass fractions $\gtrsim$1% (Ginzburg et al. 2016), such a small $f_{\mathrm{atm},0}$ for LHS 1140 b would imply formation in a gas-poor environment in less than 0.1 Myr (Lee & Connors 2021) or that it lost part of its atmosphere during giant impacts (Inamdar & Schlichting 2016). The relatively large semimajor axis of LHS 1140 b (∼0.1 au) is just beyond the instellation needed to strip the atmosphere; the final f_{atm} after 10 Gyr is close to the initial $f_{\mathrm{atm},0}$. In other words, the radius evolution over the simulation timescale is dominated by the cooling/contraction of the atmosphere.

4.2.2. Pure Rocky Planet

This is the special case of a rocky planet with no water envelope, i.e., the WMF forced to zero. With no prior on the Fe/Mg ratio, our model converges to a very small CMF ($4.3^{+4.1}_{-2.7}$%), essentially consistent with a coreless planet with a predicted Fe/Mg ratio ($0.37^{+0.12}_{-0.07}$) significantly lower (2.3σ) than observed for the host star ($1.03^{+0.40}_{-0.29}$) and much smaller than the lowest value ever measured in M dwarfs of the solar neighborhood (see Figure E1). Moreover, this model converges to a larger mass and smaller radius than observed (2.3σ offset in density). We argue that the inconsistency with the observations coupled with the challenge of forming highly iron-depleted (coreless) planets (Carter et al. 2015; Scora et al. 2020; Spaargaren et al. 2023) make this scenario implausible for LHS 1140 b. This conclusion is in line with exoplanet demographics (Rogers 2015) and the empirical rocky-to-gaseous transition around M dwarfs (Cloutier & Menou 2020) that most $\sim 1.6\,R_\oplus$ exoplanets are not rocky.

4.2.3. Water World

For this scenario, we also include an atmospheric layer, essentially a (small) fixed radius correction associated with a potential atmosphere. For the general case of a water world receiving more irradiation than the runaway greenhouse threshold ($T_{\rm eq} \gtrsim 300$ K; Turbet et al. 2020; Aguichine et al. 2021), the outer layer is likely to be supercritical, which would significantly inflate the radius, requiring a proper joint modeling of the warm water layer in the vapor/supercritical state on top of a core+mantle interior. While we defer this general case to a future publication (M. Plotnykov et al. 2024, in preparation), LHS 1140 b with a small $T_{\rm eq} = 226 \pm 6$ K does not warrant such a detailed treatment, since a potential outer water layer on this planet is most likely to be in either a frozen or a liquid state, as the planet resides in the water condensation zone (Turbet et al. 2023). We thus assume the atmospheric layer of LHS 1140 b to be an Earth-like atmosphere with a surface pressure of 1 bar and surface temperature equal to $T_{\rm eq}$. The radius correction (a few tens of kilometers) for such a thin atmosphere is negligible.

Two prior cases for the Fe/Mg abundance ratio are considered. The unconstrained case (no prior) yields CMF $=28.3^{+14.3}_{-15.9}$% and WMF $=18.7^{+12.6}_{-9.8}$%; while assuming that the planet shares the same Fe/Mg ratio as the host star (stellar prior), we obtain CMF $=20.5^{+5.5}_{-5.8}$% and WMF $= 13.7^{+5.4}_{-4.5}$%. As shown in Table 2, adopting a solar Fe/Mg ratio instead of those measured on LHS 1140 yields an even larger WMF. We tested changing the surface temperature and pressure (using climate predictions from Section 4.3) to generate a fully solid/liquid water surface. The effect of phase change is small; both CMF and WMF remained within the reported uncertainty for all models.

A variant of this model is the Hycean world (Madhusudhan et al. 2021), i.e., a water world surrounded by a thin H/He-rich layer, as was recently proposed for the temperate mini-Neptune K2-18 b (Madhusudhan et al. 2023). This new result opens the possibility that LHS 1140 b may be a lower-mass version of such a Hycean planet in the middle of the radius valley (Fulton et al. 2017). In this scenario, the lower mean molecular weight of the atmosphere yields a higher radius correction (up to 250 km for $\mu \sim 2$) corresponding to $\sim$2% of the planet radius. This case with a stellar prior on Fe/Mg still yields a significant WMF $= 9.3^{+4.6}_{-3.9}$% with CMF $= 21.7^{+5.4}_{-6.6}$%.

Table 2
Summary of the Interior Models of LHS 1140 b

Model	CMF (%)	WMF (%)	Fe/Mg [w][a]
LHS 1140			
Host star (reference)	⋯	⋯	$1.0^{+0.4}_{-0.3}$
LHS 1140 b			
Purely rocky (no prior)	$4.3^{+4.2}_{-2.7}$	—	$0.4^{+0.1}_{-0.1}$
Water world (no prior)	$28.3^{+14.3}_{-15.9}$	$18.7^{+12.6}_{-9.8}$	$1.6^{+2.5}_{-0.9}$
Water world (stellar prior)	$20.5^{+5.5}_{-5.8}$	$13.7^{+5.4}_{-4.5}$	$1.1^{+0.3}_{-0.3}$
Water world (solar prior)	$27.8^{+4.6}_{-4.2}$	$17.1^{+5.2}_{-5.0}$	$1.8^{+0.2}_{-0.2}$
Hycean world[b] (stellar prior)	$21.7^{+5.4}_{-6.6}$	$9.3^{+4.6}_{-3.9}$	$1.1^{+0.3}_{-0.3}$

Note.
[a] The Fe/Mg ratio is by weight.
[b] The Hycean model is derived from the water-world model (stellar prior) by subtracting 250 km from the planetary radius corresponding to five atmospheric scale heights of H_2.

The main conclusion from this modeling exercise summarized in Table 2 is that LHS 1140 b is unlikely to be a rocky super-Earth. The planet is either a unique mini-Neptune with a thin $\sim$0.1% H/He atmosphere or a water world with a WMF in the 9%–19% range depending on the atmospheric composition and the Fe/Mg ratio of the planetary interior. Transmission spectroscopic observations with JWST (Gardner et al. 2023) will be key to discriminating between these scenarios.

4.3. 3D GCM of LHS 1140 b and Prospects for Atmospheric Characterization

Here we consider the case of a water world with a thin atmosphere for LHS 1140 b, as this scenario presents broader implications for habitability. Planets with large amounts of water are likely to have CO_2+N_2+H_2O atmospheres (Forget & Leconte 2014; Kite & Ford 2018), possibly with high amounts of CO_2 (Marounina & Rogers 2020). While the diversity of water-world atmospheres has yet to be explored, we adopt here two distinct atmospheric compositions as a first working hypothesis and proof of concept to predict the transmission spectrum of LHS 1140 b: an Earth-like atmosphere (1 bar N_2, 400 ppm CO_2) and a CO_2-dominated atmosphere (5 bars CO_2).

The simulations were computed with the Generic Planetary Climate Model, a state-of-the-art 3D climate model (Wordsworth et al. 2011) historically known as the LMD (Laboratoire de Météorologie Dynamique, Paris, France) Generic Global Climate Model (GCM). The model has been widely applied to simulate all types of exoplanets, ranging from terrestrial planets like the TRAPPIST-1 planets (Turbet et al. 2018; Fauchez et al. 2019) to mini-Neptunes like GJ 1214 b (Charnay et al. 2015) or K2-18 b (Charnay et al. 2021). The GCM uses an up-to-date generalized radiative transfer and can simulate a wide range of atmospheric compositions (N_2, H_2O, CO_2, etc.) including clouds self-consistently.

The model was used to make realistic predictions of LHS 1140 b's atmospheric properties (temperature–pressure profile, water vapor, and cloud mixing ratios), summarized in Figure 5. We find

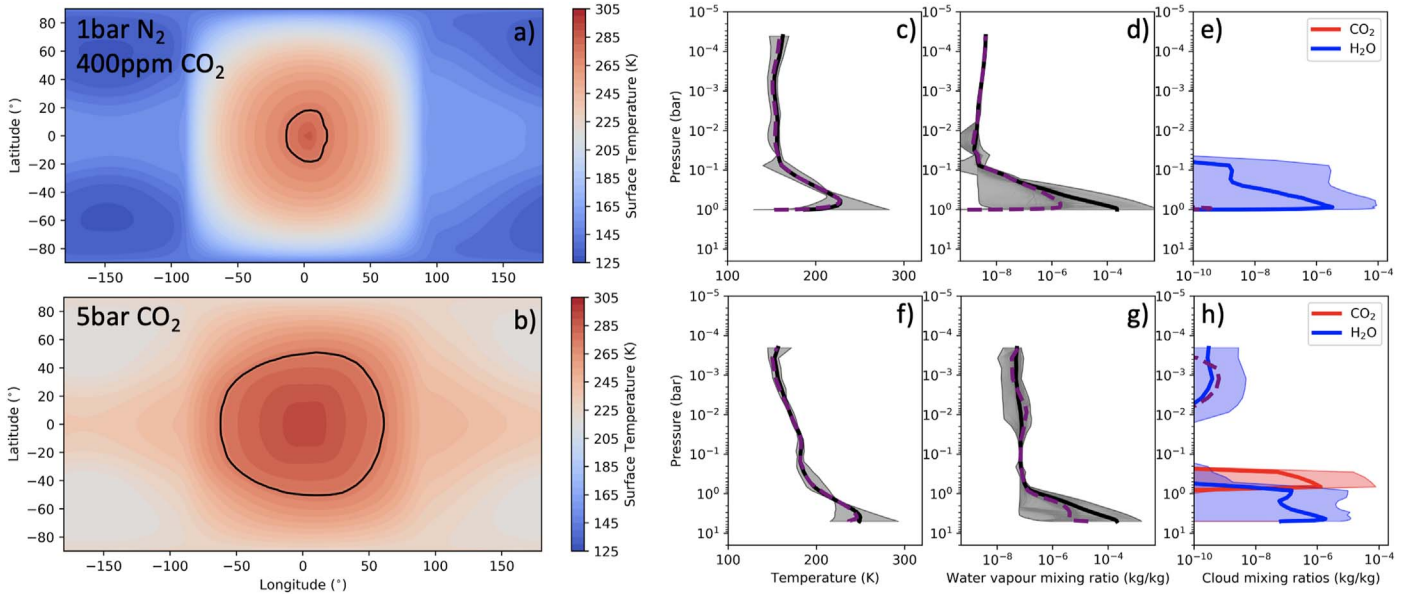

Figure 5. Results of Global Climate Model (GCM) simulations of LHS 1140 b assuming an Earth-like atmosphere (1 bar N_2, 400 ppm CO_2; panels (a), (c), (d), and (e)) and a thick CO_2-dominated atmosphere (5 bars CO_2; panels (b), (f), (g), and (h)). Panels (a) and (b): surface temperature maps of LHS 1140 b. The black line indicates the line of stability between liquid water and sea ice. The extent of the ice-free ocean strongly depends on the amount of CO_2 in the atmosphere. Panels (c)–(h): vertical profiles of the atmospheric temperatures, water vapor, and cloud mixing ratios (both H_2O and CO_2 ice clouds). The thick solid lines indicate the global mean vertical profiles, and the dotted lines indicate the terminator vertical profiles (impacting transit spectra).

that no matter how much CO_2 is included in the model, the planet has a patch of liquid water at the substellar point. The extent of the ice-free ocean grows with increasing atmospheric CO_2 due to the greenhouse effect. This result is similar to that shown by Turbet et al. (2016), Boutle et al. (2017), and Del Genio et al. (2018) for Proxima b and Wolf et al. (2017), Turbet et al. (2018), and Fauchez et al. (2019) for the TRAPPIST-1 planets: water worlds synchronously rotating in the HZ of low-mass stars almost always have surface liquid water, at least at the substellar point.

Note that the GCM simulations presented here do not include dynamic ocean and sea ice transport, which could slightly change the extent of the substellar liquid water ocean depending on the amount of CO_2 (Del Genio et al. 2019; Yang et al. 2020). Note also that we assumed that LHS 1140 b is in synchronous rotation. This is the most likely rotation mode given LHS 1140 b's proximity to its star and low eccentricity (Ribas et al. 2016), producing gravitational tides that are expected to dominate atmospheric tides for this planet (Leconte et al. 2015).

The outputs of the GCM were used to compute realistic transmission spectra that take into account the 3D nature of the atmosphere. We used the Planetary Spectrum Generator (Villanueva et al. 2018, 2022) to produce transmission spectrum models (following the methodology of Fauchez et al. 2019) of LHS 1140 b based on the output of the two GCM simulations including the effects of H_2O/CO_2 clouds. As shown in Figure 6, the strongest atmospheric feature predicted by these models is CO_2 near 4.3 μm with a strength of about 15 ppm. Changing the partial pressure of CO_2 from 400 ppm to 5 bars produces a similar CO_2 bump, as this molecule essentially condenses at higher concentration to form ice particles at low altitude (see Figure 5(h)).

LHS 1140 b was observed twice in transit with JWST in 2023 July during Cycle 1 (PID: 2334; PI: M. Damiano, unpublished). The two visits were made with NIRSpec (Böker et al. 2023) using the Bright Object Time Series mode, one transit with the G235H disperser (1.66–3.05 μm) and the other with G395H (2.87–5.14 μm). We used `PandExo` (Batalha et al. 2017) to simulate NIRSpec observations, keeping the same observing strategy of alternating between G235H and G395H. For a degraded spectral resolution of $R \simeq 20$ and assuming a conservative 5 ppm noise floor (Coulombe et al. 2023), these simulations predict a sensitivity of about 20 ppm for G235H/G395H per spectral bin and per transit. As shown in Figure 6, the Cycle 1 data have the capability to identify the mini-Neptune scenario, but should LHS 1140 b be a water world, we predict that an additional 18 transits (20 in total) would be required to detect its atmosphere (at 4σ). This estimation is made by simulating 1000 transmission spectra and comparing the log Bayesian evidence ($\ln Z$) between a flat spectrum and the Earth-like model of Figure 6 with the median simulation shown in the same figure yielding $\Delta \ln Z = 6.5$ or 4σ (Benneke & Seager 2013). Note that the optimal observing strategy has yet to be fine-tuned depending on the level of stellar contamination yet to be characterized. This may warrant some visits being obtained regularly with NIRISS SOSS (0.6–2.8 μm; Albert et al. 2023; Doyon et al. 2023).

It should be noted that only four transits are observable every year with JWST as a result of the 24.7 day period of LHS 1140 b and the fact that the system is near the ecliptic. An in-depth atmospheric characterization will realistically require that all future transit events of this planet be observed with JWST over several years (at least 3 yr to detect a 15 ppm CO_2 signal at 3σ). Irrespective of the nature of LHS 1140 b, we advocate initiating an extensive campaign as soon as possible, considering the uniqueness of this temperate world.

5. Summary and Conclusion

In this letter, we revisited the M4.5 LHS 1140 system hosting two transiting small exoplanets, including LHS 1140 b in the HZ. We applied the novel LBL precision RV method of Artigau et al. (2022) to publicly available ESPRESSO data,

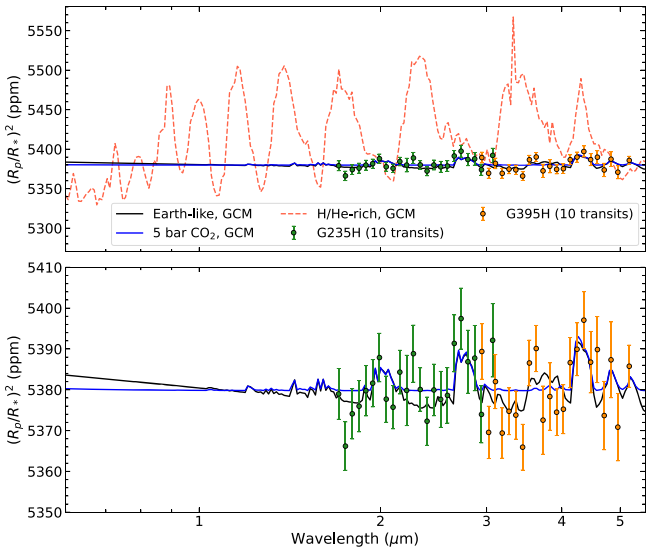

Figure 6. Predicted transmission spectrum of LHS 1140 b from 0.6 to 5.5 μm for the Earth-like (black) and 5 bar CO_2 (blue) global climate models (GCM, Figure 5). The bottom panel is a zoom of the top panel. Simulated JWST/NIRSpec data with the G235H (green) and G395H (orange) dispersers are shown. We estimate that 20 transits equally divided between G235H and G395H are required to detect a secondary atmosphere around LHS 1140 b at 4σ. The red dashed curve is a GCM-based representation of a mini-Neptune (H/He-rich) that can be easily detected with a single visit.

previously analyzed by Lillo-Box et al. (2020) using the CCF technique. The improvement on the RVs is significant; the errors are reduced by almost a factor of 3, the residual dispersion is halved, and no important excess white noise is detected. By jointly fitting the RVs with transits from Spitzer (three new archival transits), HST, and TESS (new sector 30), we update the planetary mass and radius to $5.60 \pm 0.19\,M_\oplus$ and $1.730 \pm 0.025\,R_\oplus$ for LHS 1140 b and $1.91 \pm 0.06\,M_\oplus$ and $1.272 \pm 0.026\,R_\oplus$ for LHS 1140 c. The improved RV data do not support the existence of the nontransiting candidate LHS 1140 d announced by Lillo-Box et al. (2020).

Our revised mass and radius measurements reveal that LHS 1140 b is unlikely to be a rocky super-Earth, as previously reported, as it would require (1) a density larger (by 2.3σ) than observed, (2) a CMF consistent with a coreless planet (CMF = $4.3^{+4.2}_{-2.7}$%), and (3) a planetary Fe/Mg weight ratio smaller (2.3σ) than measured on its host star and never measured in any solar neighborhood M dwarfs. Instead, our analysis shows that LHS 1140 b could be either one of the smallest known mini-Neptunes (~0.1% H/He by mass) with an atmosphere stable to mass loss over the lifetime of the system or a water world with a significant WMF of $13.7^{+5.5}_{-4.5}$% when the iron-to-magnesium weight ratio of the planet is informed by those measured with NIRPS on the host star (Fe/Mg = $1.03^{+0.40}_{-0.29}$). For LHS 1140 c, our updated density is consistent with a rocky world depleted in iron relative to Earth's, but this result is highly influenced by radius measurements that are currently discrepant between Spitzer and TESS to 4σ.

We recommend in-depth transit spectroscopy with JWST to characterize the atmosphere on LHS 1140 b, which we predict would create a CO_2 feature at 4.3 μm potentially as small as ~15 ppm according to self-consistent 3D global climate modeling of the planet in the water-world hypothesis. These simulations show that the atmospheric CO_2 concentration controls the surface temperature and the extent of a liquid water ocean. For an Earth-like case (1 bar N_2, 400 ppm CO_2), liquid water is limited to a small patch at the substellar point, while for a CO_2-dominated atmosphere (5 bars CO_2), almost a whole hemisphere is covered. These future observations could reveal the first exoplanet with a potentially habitable atmosphere and surface.

Acknowledgments

We thank the anonymous referee for constructive comments and suggestions that improved the presentation of this letter.

This study uses public ESPRESSO data under program IDs 0102.C-0294(A), 0103.C-0219(A), and 0104.C-0316(A) (PI: J. Lillo-Box).

This work is partly supported by the Natural Science and Engineering Research Council of Canada and the Trottier Institute for Research on Exoplanets through the Trottier Family Foundation.

We acknowledge the use of public TESS Alert data from pipelines at the TESS Science Office and the TESS Science Processing Operations Center. Resources supporting this work were provided by the NASA High-End Computing (HEC) Program through the NASA Advanced Supercomputing (NAS) Division at Ames Research Center for the production of the SPOC data products. This letter includes data collected by the TESS mission that are publicly available from the Mikulski Archive for Space Telescopes (MAST).

This work has been carried out within the framework of the NCCR PlanetS supported by the Swiss National Science Foundation (SNSF) under grants 51NF40_182901 and 51NF40_205606. This project has received funding from the SNSF for project 200021_200726. F.P. would like to acknowledge the SNSF for supporting research with ESPRESSO and NIRPS through grant Nos. 140649, 152721, 166227, 184618, and 215190.

This project has received funding from the European Research Council (ERC) under the European Union's Horizon 2020 research and innovation program (grant agreement SCORE No. 851555).

Cofunded by the European Union (ERC, FIERCE, 101052347). The views and opinions expressed are, however, those of the author(s) only and do not necessarily reflect those of the European Union or the European Research Council. Neither the European Union nor the granting authority can be held responsible for them.

M.T. thanks the Gruber Foundation for its generous support of this research, support from the Tremplin 2022 program of the Faculty of Science and Engineering of Sorbonne University, and the Generic PCM team for the teamwork development and improvement of the model. This work was performed using the High-Performance Computing (HPC) resources of Centre Informatique National de l'Enseignement Supérieur (CINES) under allocation Nos. A0100110391 and A0120110391 made by Grand Équipement National de Calcul Intensif (GENCI).

T.J.F. acknowledges support from the GSFC Sellers Exoplanet Environments Collaboration (SEEC), which is funded in part by the NASA Planetary Science Division's Internal Scientist Funding Model.

R.A. is a Trottier Postdoctoral Fellow and acknowledges support from the Trottier Family Foundation. This work was supported in part through a grant from the Fonds de Recherche du Québec—Nature et Technologies (FRQNT).

J.I.G.H., V.M.P., and A.S.M. acknowledge financial support from Spanish Ministry of Science and Innovation (MICINN) project PID2020-117493GB-I00 and A.S.M. from Government of the Canary Islands project ProID2020010129.

This work was supported by Fundação para a Ciência e a Tecnologia (FCT) through national funds and FEDER through COMPETE2020—Programa Operacional Competitividade e Internacionalização by these grants: UIDB/04434/2020, UIDP/04434/2020. The research leading to these results has received funding from the European Research Council through grant agreement 101052347 (FIERCE). E.D.M. acknowledges the support from Stimulus FCT contract 2021.01294.CEECIND and by the following grants: UIDB/04434/2020, UIDP/04434/2020, and 2022.04416.PTDC.

B.L.C.M. and J.R.M. acknowledge continuous grants from the Brazilian funding agencies CNPq and Print/CAPES/UFRN. This study was financed in part by the Coordenação de Aperfeiçoamento de Pessoal de Nível Superior—Brasil (CAPES)—Finance Code 001.

T.H. acknowledges support from an NSERC Alexander Graham Bell CGS-D scholarship.

X.D. acknowledges support by the French National Research Agency in the framework of the Investissements d'Avenir program (ANR-15-IDEX-02), through the funding of the "Origin of Life" project of the Grenoble-Alpes University.

Facilities: Spitzer, HST, TESS, ESO-VLT/ESPRESSO, ESO-La Silla/NIRPS.

Software: `emcee` (Foreman-Mackey et al. 2013); `Astropy` (Astropy Collaboration et al. 2018); `radvel` (Fulton et al. 2018); `matplotlib` (Hunter 2007); `juliet` (Espinoza et al. 2019); `batman` (Kreidberg 2015); `SciPy` (Virtanen et al. 2020); `NumPy` (Harris et al. 2020); `zeus` (Karamanis et al. 2021); `seaborn` (Waskom 2021); `exofile` (github.com/AntoineDarveau/exofile); `corner` (Foreman-Mackey 2016); `PSG` (Villanueva et al. 2022).

Appendix A
Light Curves

In this appendix, we present the light curves of LHS 1140 from Spitzer, HST, and TESS. The four individual transits of LHS 1140 b and one of LHS 1140 c acquired with Spitzer are presented in Figure A1. The single transit visit from HST with the WFC3 (white light curve) is shown in Figure A2. Lastly, the full TESS light curves from sectors 3 and 30 are presented in Figure A3.

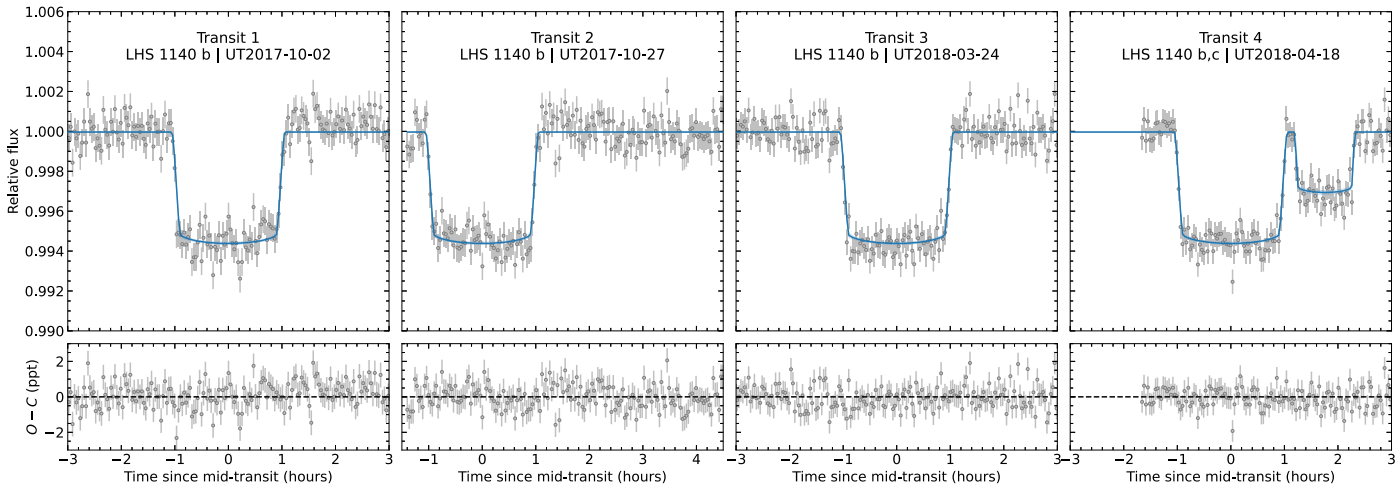

Figure A1. Individual Spitzer transits of LHS 1140 b (transits 1–4) and c (transit 4 only). The best-fit transit models of the planets are shown in blue, with the residual of the fit shown below.

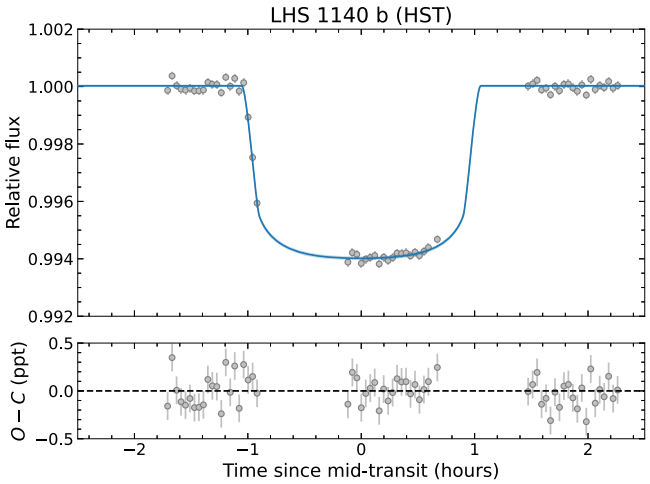

Figure A2. White light curve transit of LHS 1140 b with the WFC3 on HST. The best-fit transit model is shown in blue, with the residuals of the fit shown in the bottom panel.

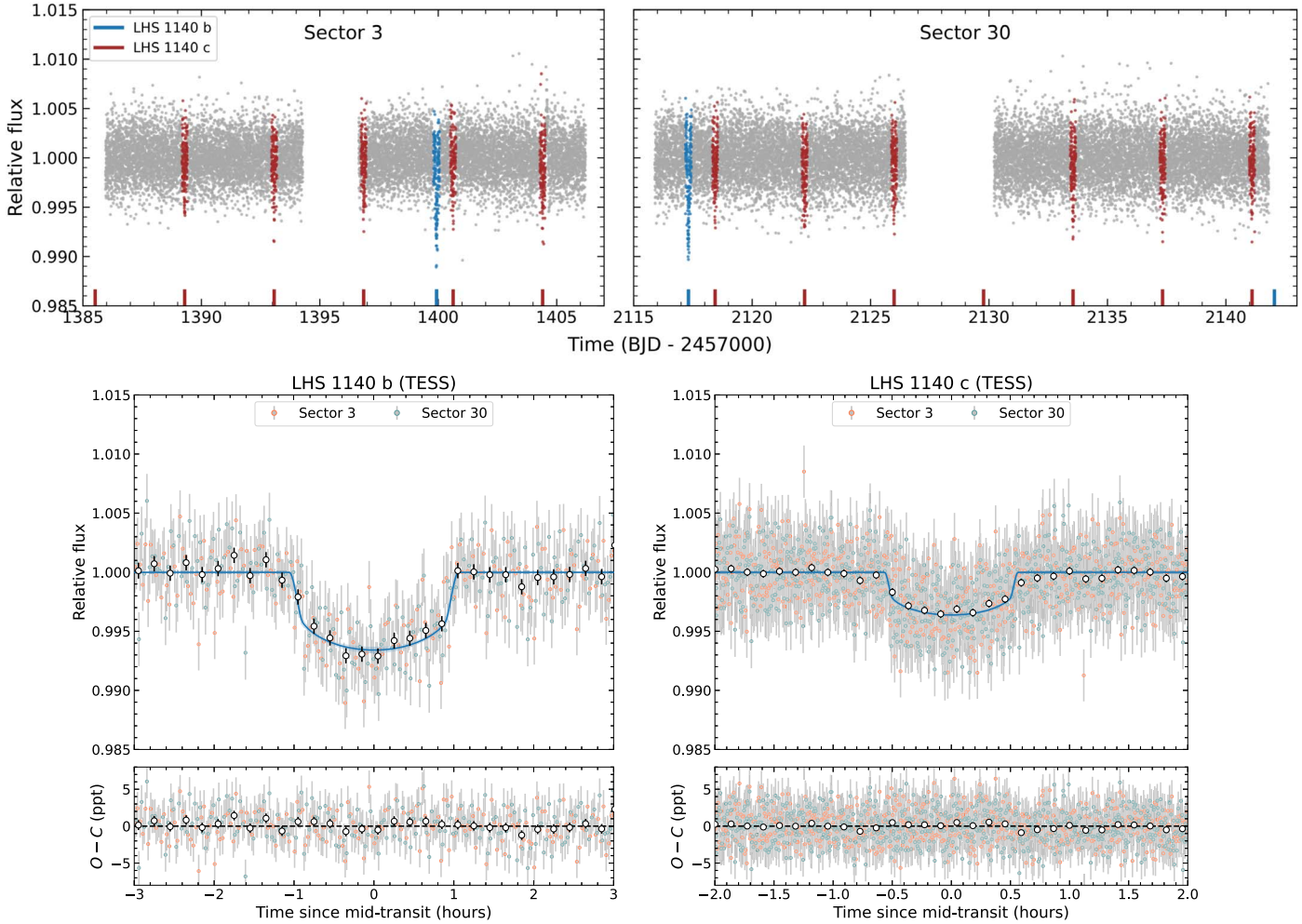

Figure A3. Top panels: normalized PDCSAP light curve of LHS 1140 from TESS sectors 3 and 30. The blue and red vertical ticks and data points highlight the transits of planet b and c. Bottom panels: phase-folded transit of LHS 1140 b (left) and c (right). The open circles represent the binned photometry, respectively, 12 and 8 minute bins for b and c. The best-fit transit models are depicted with blue curves. The residuals of the fits are shown below their respective transit.

Appendix B
RV Measurements

The ESPRESSO RVs of LHS 1140 extracted with the LBL method are shown in Figure B1 and listed in Table B1, fully available online.

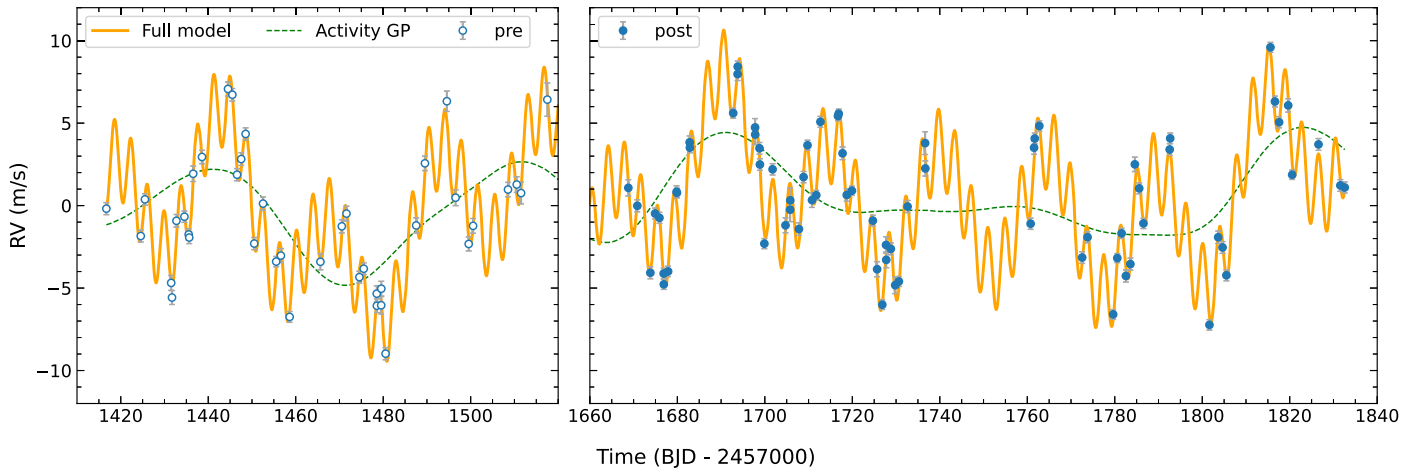

Figure B1. RV time series of LHS 1140 with ESPRESSO produced with the LBL method. The data before (pre) and after (post) the fiber upgrade of ESPRESSO (2019 June) are distinguished with open and filled circles, respectively. The full RV model (planet b, planet c, and activity GP) is represented by an orange curve, with the activity GP component highlighted with a green dashed curve (details in Appendix D.1).

Table B1
ESPRESSO RV of LHS 1140 Obtained with the LBL Method

BJD–2400000	RV ($m\,s^{-1}$)	σ_{RV} ($m\,s^{-1}$)
58416.711656	−13,457.505	0.364
58424.576752	−13,459.164	0.360
58425.528804	−13,456.943	0.343
58431.527205	−13,462.007	0.453
58431.714392	−13,462.893	0.423
58432.733559	−13,458.241	0.383
58434.555946	−13,457.993	0.346
…	…	…

(This table is available in its entirety in machine-readable form.)

Appendix C
Supplementary Material of the Stellar Characterization

C.1. Stellar Age

We analyzed the kinematics of LHS 1140 to characterize its age. This was done by assessing whether the star belongs to the Galaxy's thin or thick disk stellar populations; thick disk stars are older (∼10 Gyr) than their counterparts in the thin disk, have different chemistry ([Fe/H] ∼ −0.5, [α/Fe] ∼ +0.3; Reddy et al. 2006), and are kinematically hotter, with larger velocity dispersions relative to the local standard of rest (LSR) and larger orbital excursions from the Galactic midplane (Binney & Tremaine 2008). We employed the astrometric solution from Gaia DR3 (Gaia Collaboration et al. 2023). We note that the solution's renormalized unit weight error `ruwe` = 1.53 indicates that there is some uncertainty in the astrometry (`ruwe` $\lesssim$ 1.4 for well-behaved solutions; Lindegren 2018). The orbit of LHS 1140 was integrated forward in time 60 Myr using the Monte Carlo model outlined in Hallatt & Wiegert (2020).

These calculations produce a velocity with respect to the LSR (U_{LSR}, V_{LSR}, W_{LSR}) = (14.38 ± 0.041, −38.52 ± 0.09, 11.18 ± 0.41) $km\,s^{-1}$, yielding $V_{tot} = \sqrt{U_{LSR}^2 + V_{LSR}^2 + W_{LSR}^2}$ = 42.61 ± 0.20 $km\,s^{-1}$ (adopting the LSR from Bland-Hawthorn & Gerhard 2016). This places LHS 1140 in the thin disk, where $V_{tot,thin} \lesssim 50\,km\,s^{-1}$ (e.g., Bensby et al. 2003; Hawkins et al. 2015). Its orbital oscillation amplitude above/below the Galactic midplane is 131 ± 5 pc, significantly smaller than that of thick disk stars (∼1 kpc; e.g., Li & Zhao 2017) and consistent with that of thin disk stars ∼a few Gyr old (see Figure 20 of Kordopatis et al. 2023). This result for the age of LHS 1140 is consistent with D17 (>5 Gyr) estimated from its slow rotation period and absence of Hα emission. We thus adopt that LHS 1140 has a relatively old age of >5 Gyr and is a thin disk star.

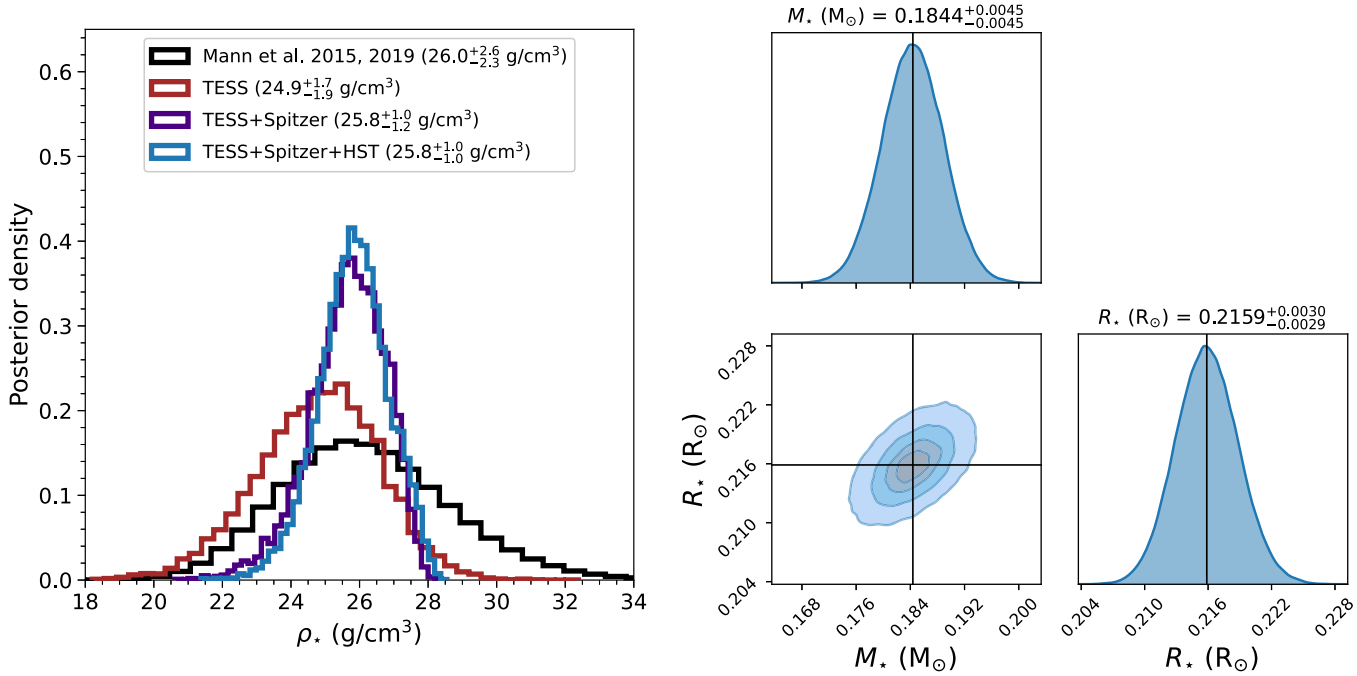

Figure C1. Left panel: stellar density ($\rho_\star$) distribution of LHS 1140 using mass and radius from Mann et al. (2015, 2019; black) and posterior distributions of $\rho_\star$ inferred from TESS (red), TESS+Spitzer (purple), and TESS+Spitzer+HST (blue) transits. Right panel: Bayesian inference of the stellar mass and radius of LHS 1140 using the TESS+Spitzer+HST constraints on $\rho_\star$ as a measurement and Mann et al. (2015, 2019) as a prior. The positive covariance in $M_\star$–$R_\star$ space indicates that both parameters are likely to vary in the same direction to produce a constant $\rho_\star$ constrained by the transits.

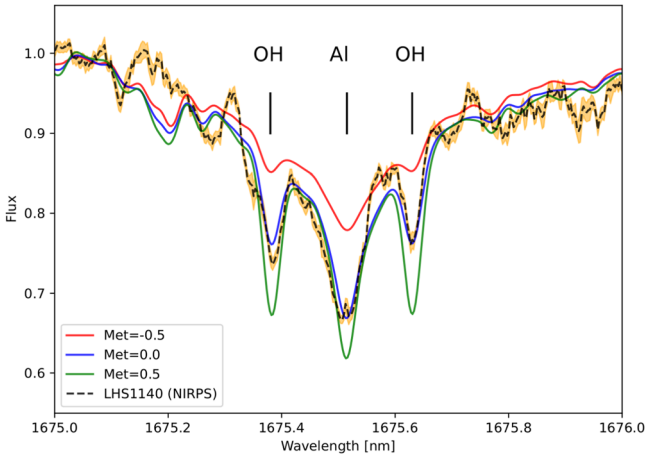

Figure C2. NIRPS template spectrum of LHS 1140 (black dashed line) around the Al I line (1675.514 nm). The orange envelope depicts the flux dispersion measured on 29 individual observations. Three ACES models with a fixed $T_{\rm eff} = 3100$ K and metallicities of −0.5 (red line), 0.0 (blue line), and 0.5 (green line) dex are shown. For this single line, we measure [Al/H] = 0.0 ± 0.1 dex. This figure illustrates the precision of the NIRPS data to constrain elemental abundances that are often different from that of iron ([Fe/H] = −0.15 ± 0.09 dex).

Table C1
LHS 1140 Stellar Parameters

Parameter	Value	References
	Astrometry and Kinematics	
R.A. (J2016.0)	00:44:59.33	(1)
Decl. (J2016.0)	−15:16:17.54	(1)
$\mu_\alpha \cos\delta$ (mas yr^{-1})	318.152 ± 0.049	(1)
μ_δ (mas yr^{-1})	−596.623 ± 0.054	(1)
π (mas)	66.8287 ± 0.0479	(1)
d (pc)	14.9636 ± 0.0107	(1)
U (km s^{-1})	14.38 ± 0.041	(2)
V (km s^{-1})	−38.52 ± 0.09	(2)
W (km s^{-1})	11.18 ± 0.41	(2)
	Physical Parameters	
$M_\star$ ($M_\odot$)	0.1844 ± 0.0045	(2)
$R_\star$ ($R_\odot$)	0.2159 ± 0.0030	(2)
$\rho_\star$ (g cm^{-3})	25.8 ± 1.0	(3)
$T_{\rm eff}$ (K)	3096 ± 48	(2)
$L_\star$ ($L_\odot$)	0.0038 ± 0.0003	(3)
SpT	M4.5V	(4)
[Fe/H] (dex)	−0.15 ± 0.09	(2)
log g (cgs)	5.041 ± 0.016	(3)
Age	>5 Gyr	(4)
$P_{\rm rot}$ (days)	131 ± 5	(4)

References. (1) Gaia DR3 (Gaia Collaboration et al. 2021); (2) this work; (3) this work derived from $M_\star$, $R_\star$, and $T_{\rm eff}$; (4) D17.

C.2. Bayesian Inference of Stellar Mass and Radius from Transits

Measured directly from transit light curves, the orbital period (P) and the scaled semimajor axis ($a/R_\star$) of an exoplanet allow the determination of the density of its host star (Seager & Mallén-Ornelas 2003):

$$\rho_{\star,\rm transit} = \frac{3\pi}{GP^2}\left(\frac{a}{R_\star}\right)^3. \quad \text{(C1)}$$

While Equation (C1) is fundamentally true for all orbits, as it is essentially a reformulation of Kepler's Third Law (with G the gravitational constant), the $a/R_\star$ inferred from transit can be significantly biased when assuming a circular orbit (e.g., Kipping 2010, 2014 Dawson & Johnson 2012). Following the notation of Van Eylen & Albrecht (2015), the true stellar density

Table C2
LHS 1140 Stellar Abundances Measured with NIRPS for Various Chemical Species with Important Features in the Near-infrared

Element	[X/H]	σ	No. of Lines
Fe I	−0.15	0.09	3
Al I	0.00	0.10	2
Mg I	0.11	0.10	2
Si I	−0.20	0.10	1
Ca I	0.20	0.10	1
O I[a]	0.00	0.01	82
C I	0.10	0.10	3
$\langle\rangle$[b]	0.01	0.04	⋯

Notes.
[a] The oxygen abundance is inferred from OH lines.
[b] Average abundance of all elements.

Table C3
LHS 1140 Stellar Abundance Weight Ratios[a]

Ratios	LHS 1140	Sun[b]	M Dwarf[c]
Fe/Mg [w][d]	$1.03^{+0.40}_{-0.29}$	1.87 ± 0.22	[0.89, 2.92]
Mg/Si [w]	$1.94^{+0.79}_{-0.56}$	0.95 ± 0.09	[0.69, 1.66]
Fe/O [w]	$0.15^{+0.04}_{-0.03}$	0.21 ± 0.03	[0.08, 0.28]
C/O [w]	$0.56^{+0.17}_{-0.13}$	0.44 ± 0.06	[0.21, 0.60]

Notes.
[a] Weight ratios calculated using X/Y [w] $= 10^{A(X)}/10^{A(Y)} \times (m_X/m_Y)$ with $A(X) = [X/H] + A_{solar}(X)$ the absolute logarithmic abundance, $A_{solar}(X)$ taken from Table 2 of Asplund et al. (2021), and m_X the atomic mass of element X.
[b] Solar weight ratios from Asplund et al. (2021).
[c] The 95% confidence interval of the M dwarf population (∼1000) of APOGEE DR16 (Majewski & APOGEE Team 2016; Ahumada et al. 2020).
[d] The Fe/Mg ratio is by weight.

($\rho_\star$) when photoeccentric effects are considered is given by

$$\frac{\rho_\star}{\rho_{\star,\mathrm{transit}}} = \frac{(1-e^2)^{3/2}}{(1+e\sin\omega)^3}, \tag{C2}$$

where e and ω are, respectively, the orbital eccentricity and argument of periastron of the transiting planet. Unaccounted eccentricity as small as $e \sim 0.1$ can potentially induce a 30% error in $\rho_\star$. From our joint transit RV analysis (Appendix D.1), we measure a $\rho_\star/\rho_{\star,\mathrm{transit}}$ of 1.00 ± 0.03 for LHS 1140 b and 1.02 ± 0.04 for LHS 1140 c, consistent with perfectly circular orbits ($e_b < 0.043$, $e_c < 0.050$ with 95% confidence). As both orbital solutions satisfy $\rho_\star \approx \rho_{\star,\mathrm{transit}}$, we hereafter drop the transit subscript when referring to stellar density obtained from our transit light curves. As summarized in Figure C1, our measurement of $\rho_\star$ constrained by Spitzer, HST, and TESS has resulted in new posteriors for the mass and radius of the star LHS 1140, namely, $M_\star = 0.1844 \pm 0.0045\ M_\odot$ and $R_\star = 0.2159 \pm 0.0030\ R_\odot$. This Bayesian approach is taken to improve the precision on $M_\star$ and $R_\star$, otherwise the dominant sources of uncertainty for the inferred planetary mass and radius.

C.3. Additional Tables and Figure

We recapitulate the stellar parameters of LHS 1140 in Table C1. After, we present the stellar abundance determination from NIRPS (Section 3.2) in Table C2 and give the corresponding chemical weight ratios in Table C3. An example of this chemical spectroscopy analysis for the Al I line (1675.514 nm) is presented in Figure C2.

Appendix D
Data Analysis

D.1. Joint Transit RV Fit

The joint analysis of the photometric (Spitzer, HST, and TESS) and RV (ESPRESSO) data is done with `juliet` (Espinoza 2018), an all-in-one package that combines transit and RV modeling using `batman` (Kreidberg 2015) and `radvel` (Fulton et al. 2018) with multiple sampling options (e.g., Markov Chain Monte Carlo, MCMC, and nested sampling). Here, we select the `dynesty` (Speagle 2020) sampler in `juliet` for parameter estimations and Bayesian log-evidence ($\ln Z$) calculations relevant for model comparisons. The `dynesty` package implements dynamic nested sampling algorithms (Higson et al. 2019) designed for more efficient and robust estimations of complex posterior distributions. We follow the `dynesty` documentation[36] and choose the random slice sampling option since the number of free parameters exceeds 20.

The orbit of planet k (k: "b," "c," "d") is described by four parameters—the orbital period P_k, time of inferior conjunction $t_{0,k}$, eccentricity e_k, and argument of periastron ω_k—and one systemic parameter, the stellar density $\rho_\star$, common for all planets. For multiplanetary systems, a single $\rho_\star$ exists, which eliminates the need to fit semimajor axes ($a_k/R_\star$) for each planet (Equation (C1)). We define a Gaussian prior on the stellar density of LHS 1140 based on Mann et al. (2015, 2019): $\rho_\star \sim \mathcal{N}(26.0, 2.6^2)$ g cm^{-3}. For the transiting planets b and c, we follow the Espinoza et al. (2019) transformation of the transit impact parameter b and planet-to-star radius ratio $p = R_p/R_\star$ into r_1 and r_2 parameters to only sample physically plausible regions in b–p space. We model the baseline flux of the Spitzer, HST, and TESS light curves with the parameter M described in Espinoza (2018) and include per-instrument extra jitter terms ($\sigma_{\mathrm{Spitzer}}$, σ_{HST}, and σ_{TESS}).

Synthetic spectra of M dwarfs often show significant discrepancy with the observations (Blanco-Cuaresma 2019), implying that theoretical limb-darkening (LD) predictions may be unreliable. Patel & Espinoza (2022) have found systematic offsets between empirical quadratic LD coefficients (u_1, u_2) and theoretical predictions in the TESS bandpass of the order Δu_1, $\Delta u_2 \approx 0.2$ for cool stars similar to LHS 1140. Differing from previous transit analyses (D17; M19; LB20; Edwards et al. 2021), we do not fix or apply Gaussian priors on the LD coefficients but let them vary freely (uniform priors). The stellar LD effects in the Spitzer, HST, and TESS transits are modeled using per-instrument quadratic q_1 and q_2 parameters (Kipping 2013) constructed to only allow physical solutions for values between 0 and 1. Note that fixing the LD parameters to those measured by previous studies for the same instrument does not change the median of our $R_p/R_\star$ posteriors.

For the Keplerian component, a semiamplitude K_k for each planet is fitted, as well as instrumental RV offsets (γ_{pre}, γ_{post}) and extra white-noise terms (σ_{pre}, σ_{post}) for ESPRESSO pre- and post-fiber upgrade. When testing for possible eccentric

[36] dynesty.readthedocs.io/en/stable/index.html

Table D1
Planetary Parameters Derived from the Joint Transit RV Fit

Parameter	LHS 1140 b	LHS 1140 c	Description
	Orbital Parameters		
P (days)	24.73723 ± 0.00002	3.777940 ± 0.000002	Period
t_0 (BJD–2457000)	1399.9300 ± 0.0003	1389.2939 ± 0.0002	Time of inferior conjunction
a (au)	0.0946 ± 0.0017	0.0270 ± 0.0005	Semimajor axis
i (deg)	89.86 ± 0.04	$89.80^{+0.14}_{-0.19}$	Inclination
e	<0.043 (95%)	<0.050 (95%)	Eccentricity
	Transit Parameters		
b	$0.23^{+0.05}_{-0.07}$	$0.09^{+0.09}_{-0.06}$	Impact parameter
δ (ppt)	5.38 ± 0.06	2.90 ± 0.09	Depth
t_{14} (hr)	2.15 ± 0.05	1.13 ± 0.02	Duration
	Physical Parameters		
R_p ($R_\oplus$)	1.730 ± 0.025	1.272 ± 0.026	Radius
M_p ($M_\oplus$)	5.60 ± 0.19	1.91 ± 0.06	Mass
ρ (g cm^{-3})	5.9 ± 0.3	5.1 ± 0.4	Bulk density
S ($S_\oplus$)	0.43 ± 0.03	5.3 ± 0.4	Insolation
T_{eq} [$A_B = 0$] (K)	226 ± 4	422 ± 7	Equilibrium temperature

orbits, we uniformly sample $\sqrt{e_k}\cos\omega_k$ and $\sqrt{e_k}\sin\omega_k$ between -1 and 1. We include in `juliet` a Gaussian process (GP) to model stellar activity in the ESPRESSO RVs. Our GP implementation in `juliet` runs `george` (Ambikasaran et al. 2015) with a quasiperiodic covariance kernel (Haywood et al. 2014; Rajpaul et al. 2015),

$$k_{i,j} = A^2 \exp\left[-\frac{|t_i - t_j|^2}{2\ell^2} - \Gamma \sin^2\left(\frac{\pi|t_i - t_j|}{P_{\rm rot}}\right)\right], \quad \text{(D1)}$$

where $|t_i - t_j|$ is the time interval between data i and j, A is the amplitude of the GP, ℓ is the coherence timescale, Γ scales the periodic component of the GP, and $P_{\rm rot}$ is the stellar rotation period. We adopt a Gaussian prior on the known rotation period of the star $P_{\rm rot} \sim \mathcal{N}(131, 5^2)$ days. The priors for the other GP hyperparameters are listed in Table D2 and mostly follow the recommendation of Stock et al. (2023; GP Prior III) when the rotation period is already constrained.

We inspected three different joint models ($\mathcal{M}$):

1. two planets, LHS 1140 b and c, on circular orbits ($\mathcal{M}_{2cp}$; $e_b = e_c = 0$, $\omega_b = \omega_c = 90°$);
2. two planets, LHS 1140 b and c, on eccentric orbits ($\mathcal{M}_{2ep}$); and
3. three planets, LHS 1140 b, c, and the candidate planet d reported by LB20, on circular orbits ($\mathcal{M}_{3cp}$; $e_b = e_c = e_d = 0$, $\omega_b = \omega_c = \omega_d = 90°$)

The difference in Bayesian log-evidence ($\Delta \ln Z$) yields the probability that one model better describes the observations than another. The empirical scale of Trotta (2008; see Table 1 therein) serves to interpret the significance of $\Delta \ln Z$ and select the "best" model. A $\Delta \ln Z > 5$ constitutes "strong" evidence in favor of the model with the highest $\ln Z$. A $2.5 < \Delta \ln Z < 5$ corresponds to "moderate" evidence, but a $\Delta \ln Z \leqslant 2.5$ means that neither model should be favored. Multiple runs of each $\mathcal{M}$ were carried out with `dynesty` to verify the consistency of $\ln Z$.

For the two-planet models $\mathcal{M}_{2cp}$ and $\mathcal{M}_{2ep}$, we obtain $\Delta \ln Z = 0.8 \pm 0.9$ in favor of the circular orbit solutions (inconclusive). We report from model $\mathcal{M}_{2ep}$ upper limits on e_b and e_c (95% confidence) of 0.043 and 0.050, respectively, implying that in all likelihood, the orbits of LHS 1140 b and c are de facto circular. For this reason, we select the simpler $\mathcal{M}_{2cp}$ as the preferred model. We present the relevant planetary parameters derived from the joint transit RV fit for model $\mathcal{M}_{2cp}$ in Table D1. The priors and posteriors (16th, 50th, and 84th percentiles) of the free parameters of model $\mathcal{M}_{2cp}$ are reported in Table D2. The best-fit transit models of the Spitzer, HST, and TESS light curves are respectively shown in Figures 1, A2, and A3. The phase-folded RVs with the best-fit orbital solutions of LHS 1140 b and c are shown in Figure 2, with the full RV model (Keplerian + activity GP) presented in Figure B1. This full RV model yields a residual rms of 41 cm s^{-1} for the "pre" data, consistent with the median RV errors of 42 cm s^{-1}. For the "post" data, the residual dispersion of 54 cm s^{-1} is larger than the typical RV errors of 34 cm s^{-1} so that a $\sigma_{\rm post} = 36 \pm 6$ cm s^{-1} jitter term is needed to fully describe the scatter.

The reanalysis of the ESPRESSO data with the LBL framework is an opportunity to test the presence of the candidate LHS 1140 d on a 78.9 day orbit reported by LB20. For model $\mathcal{M}_{3cp}$, we chose the same priors on P_d, $t_{0,d}$, and K_d as in LB20, namely, $\mathcal{U}(70, 120)$ days, $\mathcal{U}(2458350, 2458400)$ BJD, and $\mathcal{U}(0, 10)$ m s^{-1}. This fit converges to a small semiamplitude of $0.9^{+0.8}_{-0.6}$ m s^{-1} and an undefined period of 87^{+14}_{-9} days for a planet d. The Bayesian log-evidence does not increase when adding a third planet with $\Delta \ln Z = -1.0 \pm 0.9$ between $\mathcal{M}_{3cp}$ and $\mathcal{M}_{2cp}$. We also reject a K_d larger than 2.21 m s^{-1} at 2σ, corresponding to the median signal detected in LB20. LHS 1140 could realistically have other planets, but given the precision of our RV measurements, we see no evidence of an additional companion sharing the parameters of candidate LHS 1140 d. In Appendix D.3, we further demonstrate that an 80 day RV signal is most likely of stellar origin.

D.2. Transit Depth Discrepancy for LHS 1140 c

In LB20, the radii of LHS 1140 b and c measured by TESS were slightly smaller (by 1.5σ and 2σ, respectively) compared with previous results by M19 obtained with Spitzer (see Figure 3). Here, our joint analysis of Spitzer, HST (for

Table D2
Prior and Posterior Distributions of the Joint Transit RV Fit

Parameter	Prior[a]	Posterior	Description
Stellar Parameters			
$\rho_\star$ (g cm^{-3})	$\mathcal{N}(26.0, 2.6^{b})$	25.8 ± 1.0	Stellar density
LHS 1140 b			
P_b (days)	$\mathcal{U}(24.7, 24.8)$	24.73723 ± 0.00002	Orbital period
$t_{0,b}$ (BJD–2457000)	$\mathcal{U}(1399.9, 1400.0)$	1399.9300 ± 0.0003	Time of inferior conjunction
$r_{1,b}$	$\mathcal{U}(0, 1)$	0.49 ± 0.03	Parameterization[b] for b and p
$r_{2,b}$	$\mathcal{U}(0, 1)$	0.0733 ± 0.0004	Parameterization[b] for b and p
K_b (m s^{-1})	$\mathcal{U}(0, 10)$	3.80 ± 0.11	RV semiamplitude
LHS 1140 c			
P_c (days)	$\mathcal{U}(3.7, 3.8)$	3.777940 ± 0.000002	Orbital period
$t_{0,c}$ (BJD–2457000)	$\mathcal{U}(1389.25, 1389.35)$	1389.2939 ± 0.0002	Time of inferior conjunction
$r_{1,c}$	$\mathcal{U}(0, 1)$	0.39 ± 0.05	Parameterization[b] for b and p
$r_{2,c}$	$\mathcal{U}(0, 1)$	0.0539 ± 0.0008	Parameterization[b] for b and p
K_c (m s^{-1})	$\mathcal{U}(0, 10)$	2.42 ± 0.07	RV semiamplitude
Photometric Parameters			
$q_{1,\mathrm{Spitzer}}$	$\mathcal{U}(0, 1)$	$0.016^{+0.018}_{-0.009}$	LD parameter[c]
$q_{2,\mathrm{Spitzer}}$	$\mathcal{U}(0, 1)$	$0.42^{+0.36}_{-0.28}$	LD parameter[c]
M_{Spitzer} (ppm)	$\mathcal{N}(0, 1000^{b})$	34 ± 23	Baseline flux
$\sigma_{\mathrm{Spitzer}}$ (ppm)	$\mathcal{LU}(1, 1000)$	15^{+57}_{-12}	Extra white noise
$q_{1,\mathrm{HST}}$	$\mathcal{U}(0, 1)$	0.28 ± 0.08	LD parameter[c]
$q_{2,\mathrm{HST}}$	$\mathcal{U}(0, 1)$	$0.12^{+0.11}_{-0.08}$	LD parameter[c]
M_{HST} (ppm)	$\mathcal{N}(0, 1000^{b})$	-25 ± 22	Baseline flux
σ_{HST} (ppm)	$\mathcal{LU}(1, 1000)$	12^{+38}_{-10}	Extra white noise
$q_{1,\mathrm{TESS}}$	$\mathcal{U}(0, 1)$	$0.33^{+0.20}_{-0.12}$	LD parameter[c]
$q_{2,\mathrm{TESS}}$	$\mathcal{U}(0, 1)$	0.56 ± 0.27	LD parameter[c]
M_{TESS} (ppm)	$\mathcal{N}(0, 1000^{b})$	9 ± 48	Baseline flux
σ_{TESS} (ppm)	$\mathcal{LU}(1, 1000)$	17^{+116}_{-14}	Extra white noise
RV Parameters			
γ_{pre} (m s^{-1})	$\mathcal{U}(-10, 10)$	1.3 ± 1.5	RV offset[d]
γ_{post} (m s^{-1})	$\mathcal{U}(-10, 10)$	-0.6 ± 1.4	RV offset[d]
σ_{pre} (m s^{-1})	$\mathcal{LU}(10^{-3}, 10)$	$0.04^{+0.18}_{-0.03}$	Extra white noise
σ_{post} (m s^{-1})	$\mathcal{LU}(10^{-3}, 10)$	0.36 ± 0.06	Extra white noise
RV Activity GP			
A (m s^{-1})	$\mathcal{LU}(10^{-3}, 10)$	$2.8^{+1.0}_{-0.6}$	Amplitude of the GP
ℓ (days)	$\mathcal{LU}(100, 1000)$	164^{+62}_{-42}	Timescale of the GP
Γ	$\mathcal{LU}(0.1, 10)$	$3.7^{+1.5}_{-1.2}$	Periodic scale of the GP
P_{rot} (days)	$\mathcal{N}(131, 5^{b})$	133 ± 3	Rotation period

Notes.
[a] $\mathcal{U}(a, b)$ is the uniform distribution between values a and b, $\mathcal{LU}(a, b)$ is the log-uniform (Jeffreys) distribution between values a and b, and $\mathcal{N}(\mu, \sigma^2)$ is the normal distribution with mean μ and variance σ^2.
[b] Parameterization of the transit impact parameter (b) and the planet-to-star radius ratio ($p = R_p/R_\star$) outlined in Espinoza (2018).
[c] q_1, q_2 are related to the quadratic LD coefficients u_1, u_2 by the transformations described in Kipping (2013).
[d] Relative to the median RV ($-13{,}458.5$ and $-13{,}450.5$ m s^{-1} for pre- and post-fiber change data).

LHS 1140 b only), and TESS data has resulted in a similar discrepancy for planet c but not for b. In Figure D1, we show the transit impact parameter (b) and scaled radius ($p = R_p/R_\star$) of LHS 1140 b and c derived from fitting each instrument independently. The b–p posteriors of LHS 1140 b agree well for all available instruments, but we detect a 4σ tension for the p of LHS 1140 c measured by Spitzer and TESS.

We remain cautious before interpreting the transit depth discrepancy of LHS 1140 c as real because we only have a single visit with Spitzer. It is possible that data reduction systematics affected the depth measurement. Nonetheless, it is worth mentioning that Spitzer channel 2 at 4.5 μm covers a strong CO_2 feature. We detect a difference of 500 ppm between the Spitzer and TESS bandpasses, meaning that if excess atmospheric absorption is causing this discrepancy, it would be readily detectable with JWST. This work calls for a better radius determination for LHS 1140 c, particularly obtaining the full near-infrared transmission spectrum of this planet with JWST to reveal its true radius that we currently report as an average between Spitzer and TESS (see "Joint" in Figure D1) and test whether its atmosphere is CO_2-rich.

D.3. Validating Genuine Keplerian Signals with LBL RV

The LBL method allows one to verify the achromaticity of the inferred semiamplitudes of the LHS 1140 planets. The three-planet model $\mathcal{M}_{3cp}$ can be applied on velocities derived

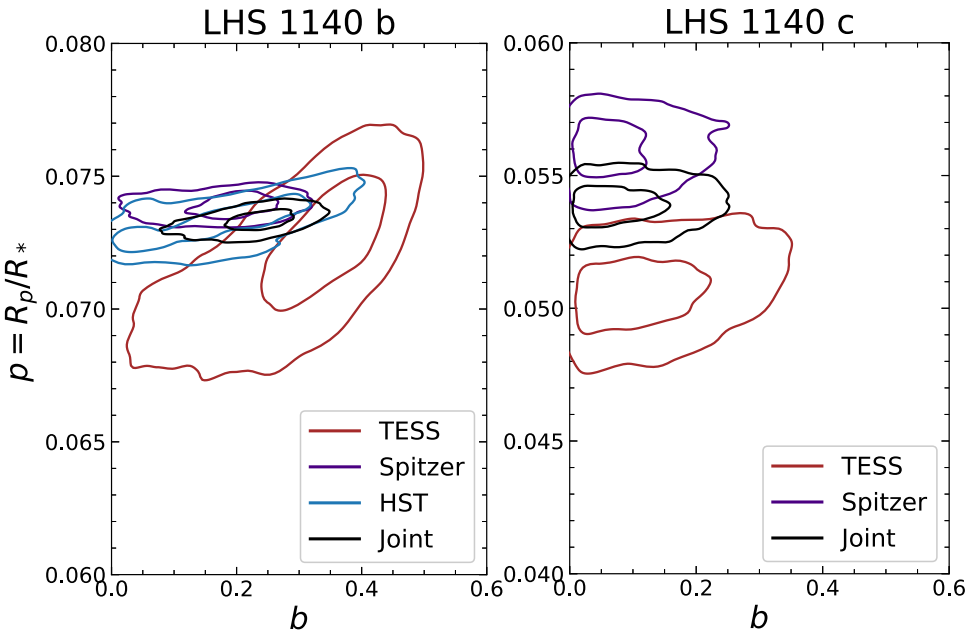

Figure D1. Posterior distributions (1σ and 2σ contours) for the transit impact parameter (b) and scaled radius ($p = R_p/R_\star$) of LHS 1140 b and c. Different colors refer to the fit on TESS (red), Spitzer (purple), and HST (blue) data only. The black contours are the final joint posteriors on all available instruments. A $\sim 4\sigma$ tension in p exists between Spitzer and TESS for LHS 1140 c.

per spectral bins of $\Delta\lambda \approx 20$ nm in the entire ESPRESSO domain. For genuine Keplerian signals:

1. (chromaticity test) the K_λ calculated for different bands are achromatic, i.e., $dK_\lambda/d\lambda = 0$;
2. (coherence test) the K_λ add constructively (coherent period and phase), yielding a consistent weighted average (value and uncertainty) with K resulting from the full spectral range; and
3. (noise test) the semiamplitude uncertainties (σ_K) should scale with RV precision ($\sigma_{\rm RV}$) according to the Cloutier et al. (2018) formalism, i.e., $\sigma_K = \sigma_{\rm RV}\sqrt{2/N_{\rm RV}}$, when no important extra jitter is detected.

These three criteria can be tested for LHS 1140 b, c, and the nontransiting candidate d. As summarized in Figure D2, we measure no chromaticity for the Keplerian signals of LHS 1140 b and c, respectively, with $dK_\lambda/d\lambda = 0.11 \pm 0.10$ and 0.03 ± 0.08 m s^{-1} per 100 nm. For the candidate LHS 1140 d, the signal is marginally larger in the blue wavelengths of ESPRESSO ($dK_\lambda/d\lambda = -0.42 \pm 0.26$ m s^{-1} per 100 nm). Similarly, since the Doppler signals of LHS 1140 b and c are perfectly coherent, the weighted average of the K_λ is consistent with the K obtained from the full spectral range (see Figure D2). This is not observed for the 80 day signal associated with candidate d for which fitting a Keplerian model on RVs derived from the full ESPRESSO wavelength range is three times less accurate. Finally, given the RV precision of this data set varying from 4.73 to 0.65 m s^{-1} in the 450–750 nm interval, we find that LHS 1140 b and c follow the Cloutier et al. (2018) formalism, but d does not (see Figure D2, right). Interestingly, the spectral interval 700–725 nm covering only 8% of the ESPRESSO domain contains 30% of all RV content of LHS 1140. The tests presented in this section provide evidence against the existence of LHS 1140 d, first announced by LB20 as a candidate nontransiting planet.

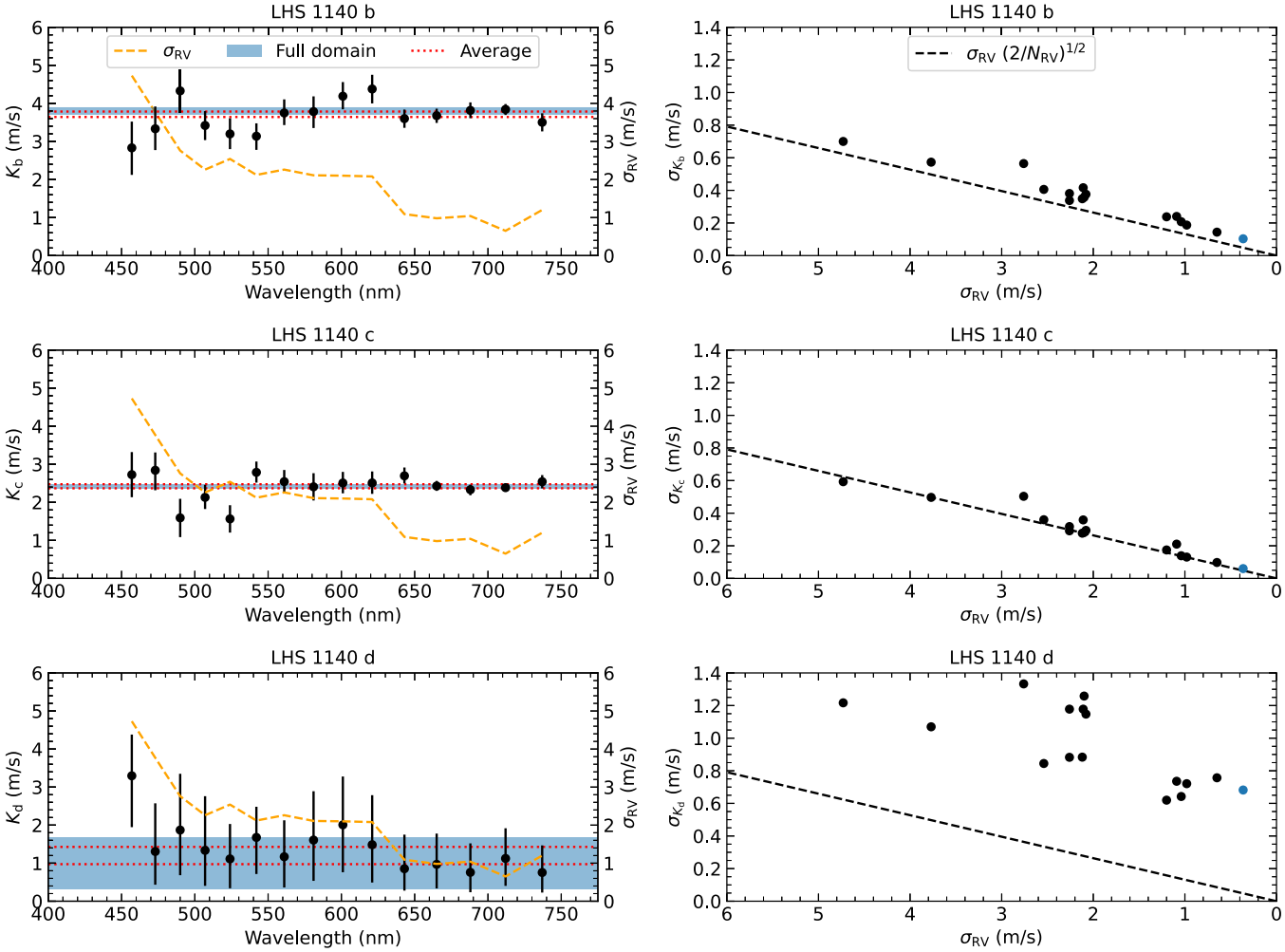

Figure D2. Validating Keplerian signals in the ESPRESSO spectral domain of LHS 1140. Left panels: semiamplitudes K_λ obtained with model $\mathcal{M}_{3cp}$ from LBL RVs extracted for different bands ($\Delta\lambda \approx 20$ nm). The per-band velocities have uncertainties (σ_{RV}) varying from 4.73 to 0.65 m s^{-1} (orange dashed lines). A genuine Keplerian signal is achromatic ($dK_\lambda/d\lambda = 0$). We measure no chromatic slopes for LHS 1140 b and c, but the signal of candidate LHS 1140 d is marginally larger in the blue wavelengths of ESPRESSO ($dK_\lambda/d\lambda = -0.42 \pm 0.26$ m s^{-1} per 100 nm). A coherent signal such as a Doppler shift affecting all wavelengths should produce consistent K between the full spectrum constraints (1σ confidence regions in blue) and the weighted average of K_λ (1σ confidence interval between the red dotted lines). Assuming a coherent signal, the K_d inferred from the full ESPRESSO domain should have an uncertainty $\sigma_{K_d} \sim 0.18$ m s^{-1}, which is inconsistent with observations. Right panels: semiamplitude uncertainties σ_K with increasing RV precision (smaller σ_{RV}). A coherent signal in wavelengths should follow the Cloutier et al. (2018) formalism ($\sigma_K = \sigma_{RV}\sqrt{2/N_{RV}}$), which is not seen for LHS 1140 d. The LBL data set shows no evidence of an 80 day signal associated with the candidate planet LHS 1140 d.

Appendix E
Supplementary Material of the Internal Structure Analysis

E.1. Interior Modeling

In this appendix, we summarize the method of Plotnykov & Valencia (2020) adapted to constrain the internal structure of LHS 1140 b.

We used a Bayesian analysis with MCMC sampling with `emcee` (Foreman-Mackey et al. 2013) coupled to the internal structure model of Valencia et al. (2007). The model assumes three layers for the interior of the planet: a condensed water (liquid/ice) layer at the surface, a mantle (Mg–Si rock), and a core (Fe–Ni–Si alloy). A fixed atmospheric layer is also considered for models in which the atmosphere could significantly contribute to the planet radius. The water layer is described by the equation of state (EOS) of Hemley et al. (1987), Wagner & Pruß (2002), and Stewart & Ahrens (2005), and we adopt the density mixing model with the EOS parameters of Stixrude & Lithgow-Bertelloni (2011) and Morrison et al. (2018) for the mantle and core, respectively. The lower mantle is assumed to be composed of bridgmanite/post-perovskite and wustite (at different proportions to that of Earth), while the upper mantle is modeled as pure olivine (Mg_2SiO_4). This choice was made in light of the possible low Si content of the star that may indicate that olivine formation is favored compared to pyroxenes ($Mg_2Si_2O_6$).

Important ingredients in the model are the abundance ratios (by weight) of refractory elements, namely, Fe/Mg and Mg/Si. We explored a no prior (Fe/Mg unconstrained) and a stellar prior (Fe/Mg following the star) model for the water-world case of LHS 1140 b (Section 4.2.3). For the pure rocky case (Section 4.2.2), the planet Fe/Mg ratio must be lower than that of the host star to produce the observed density. Consequently, only the unconstrained Fe/Mg analysis was done. Note that because we model three layers for the interior, the no prior case cannot fully constrain both the CMF and WMF; i.e., the planetary interior models are inherently degenerate in this case. For all models, the Mg/Si ratio in the mantle is assumed to be that of the host star: $\mathrm{Mg/Si_{planet}} \sim \mathcal{N}(\mathrm{Mg/Si_{star}}, \sigma^2_{\mathrm{star}})$. Despite LHS 1140 having a Mg/Si approximately twice that of the Sun/Earth (see Table C3), this ratio only weakly influences the final radius of the planet, meaning that our results do not depend on the exact mineralogy of the rocks.

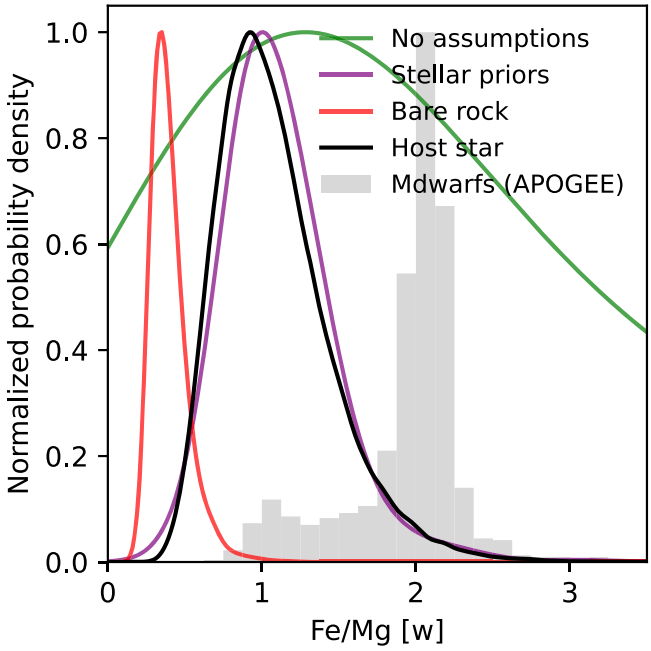

Figure E1. Fe/Mg distribution for LHS 1140 b according to different assumptions (no prior or stellar prior) for the bare-rock (red) and water-world (green and purple) models compared to the host star (black). We plot the kernel density estimate of the interior model posterior, which is normalized to have a mode of 1. We include the M dwarf distribution of Fe/Mg from the APOGEE DR16 (gray histogram, sample size of ∼1000; Majewski & APOGEE Team 2016; Ahumada et al. 2020) for comparison.

We report the posterior distributions of our interior analysis in Appendix E.2 for all interior models considered. Additionally, we compare the Fe/Mg distributions of LHS 1140 b for different scenarios in Figure E1.

E.2. Posterior Distributions

We summarize the posterior distributions of Fe/Mg for LHS 1140 b in Figure E1 for the pure rocky (Section 4.2.2) and water-world (Section 4.2.3) scenarios. The posteriors from our MCMC sampling are also presented in the corner plots of Figures E2, E3, and E4, showing the results for bare-rock, water (no prior, stellar prior, and solar prior cases), and Hycean worlds, respectively.

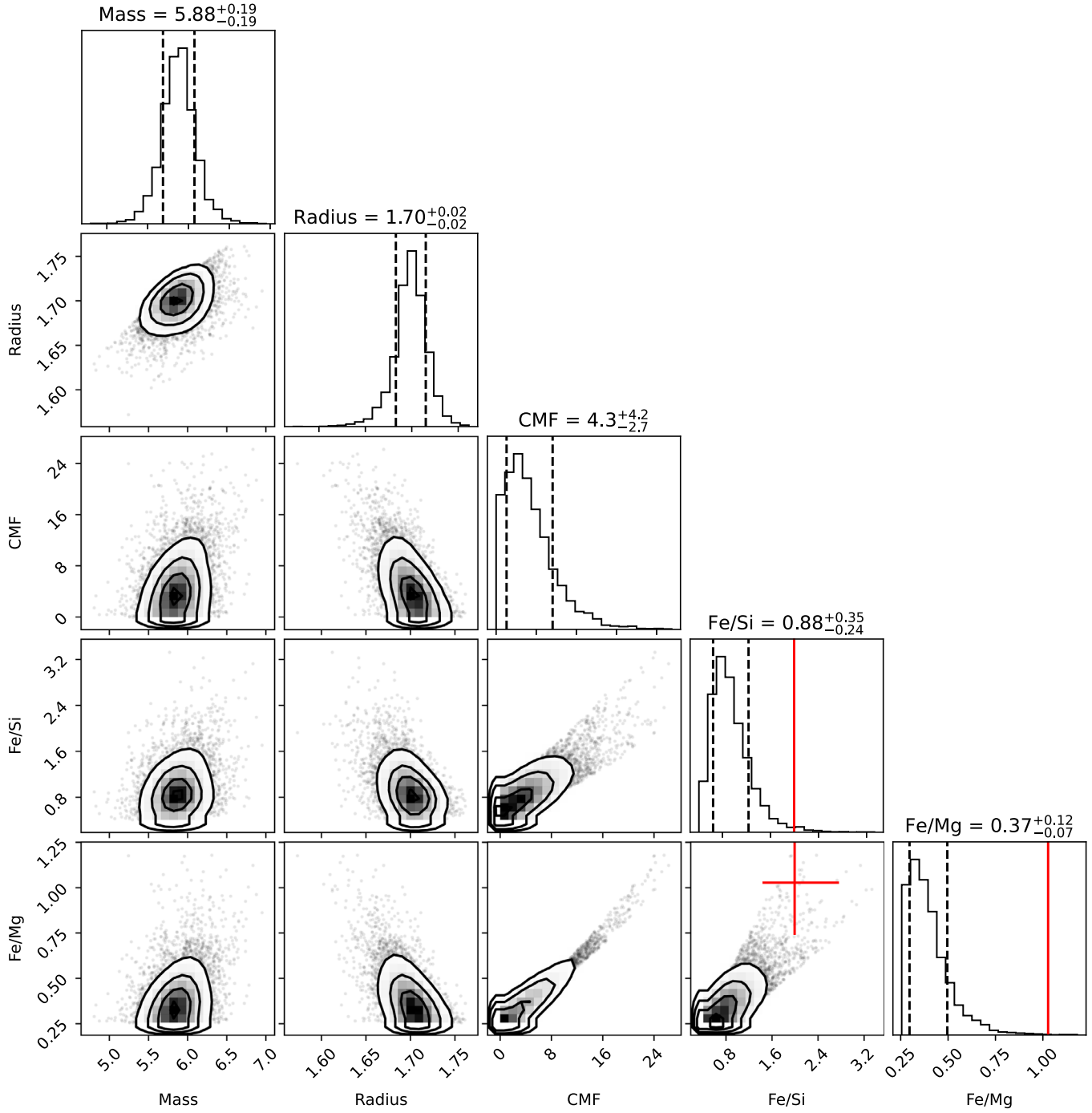

Figure E2. Posterior distribution for LHS 1140 b interior parameters for the bare-rock scenario (WMF = 0). The chemical weight ratios Fe/Si and Fe/Mg are derived quantities. The red lines (and red cross) in Fe/Si and Fe/Mg space correspond to the stellar measurements. The vertical black dashed lines represent the 16th and 84th percentiles of the posterior.

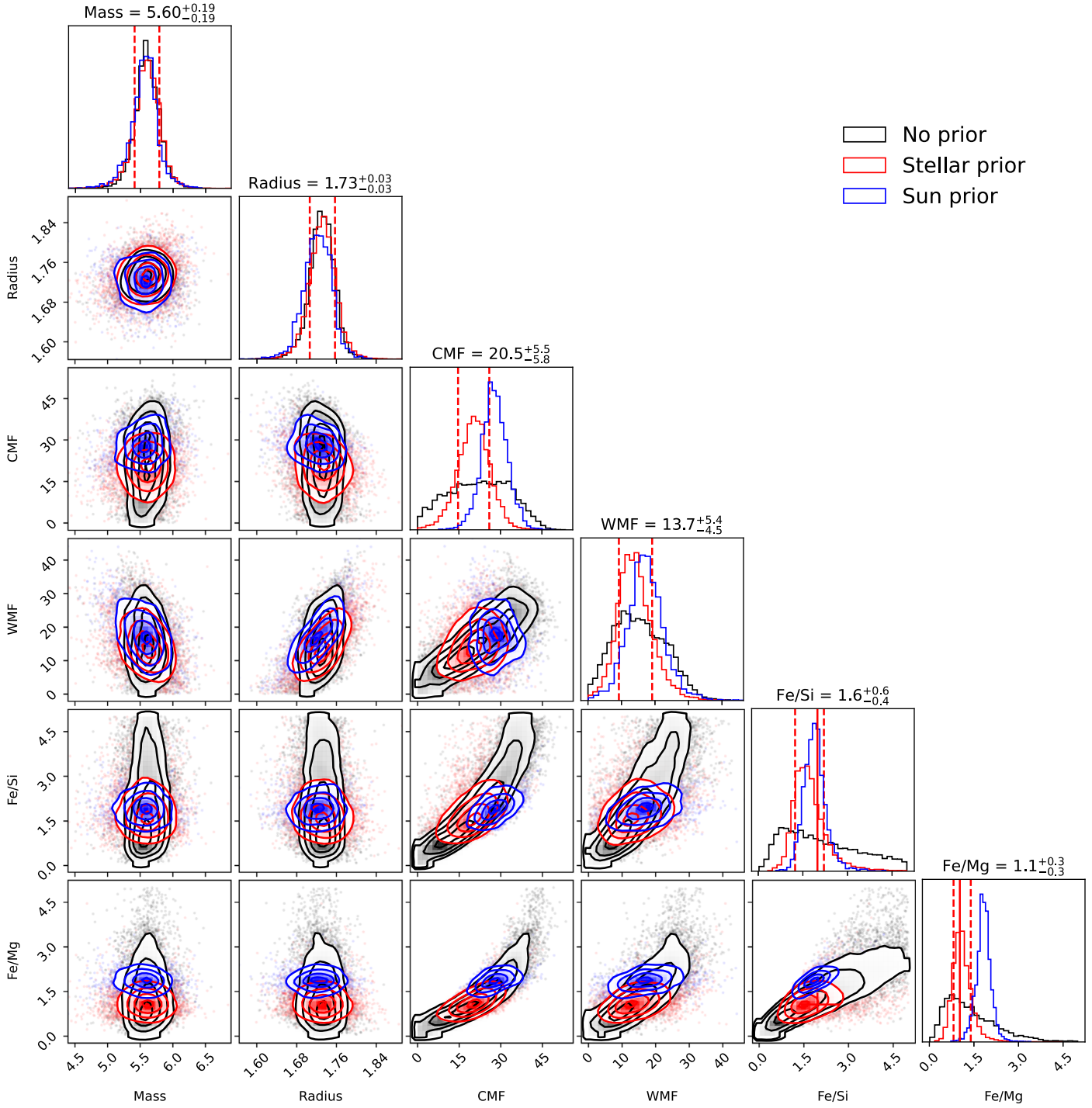

Figure E3. Posterior distribution for LHS 1140 b interior parameters for the water-world scenario (WMF > 0) for different Fe/Mg assumptions: no prior (black), stellar prior (red), and Sun prior (blue). For the stellar and Sun prior cases, the log-probability function is modified to include the restriction posed by Fe/Mg and Mg/Si ratios measured on the host star or the Sun (Table C3). The red lines (and red cross) in Fe/Si and Fe/Mg space correspond to the stellar measurements. The vertical red dashed lines represent the 16th and 84th percentiles of the posterior for the stellar prior case. Note that the values in the parameter titles are for the stellar prior case only.

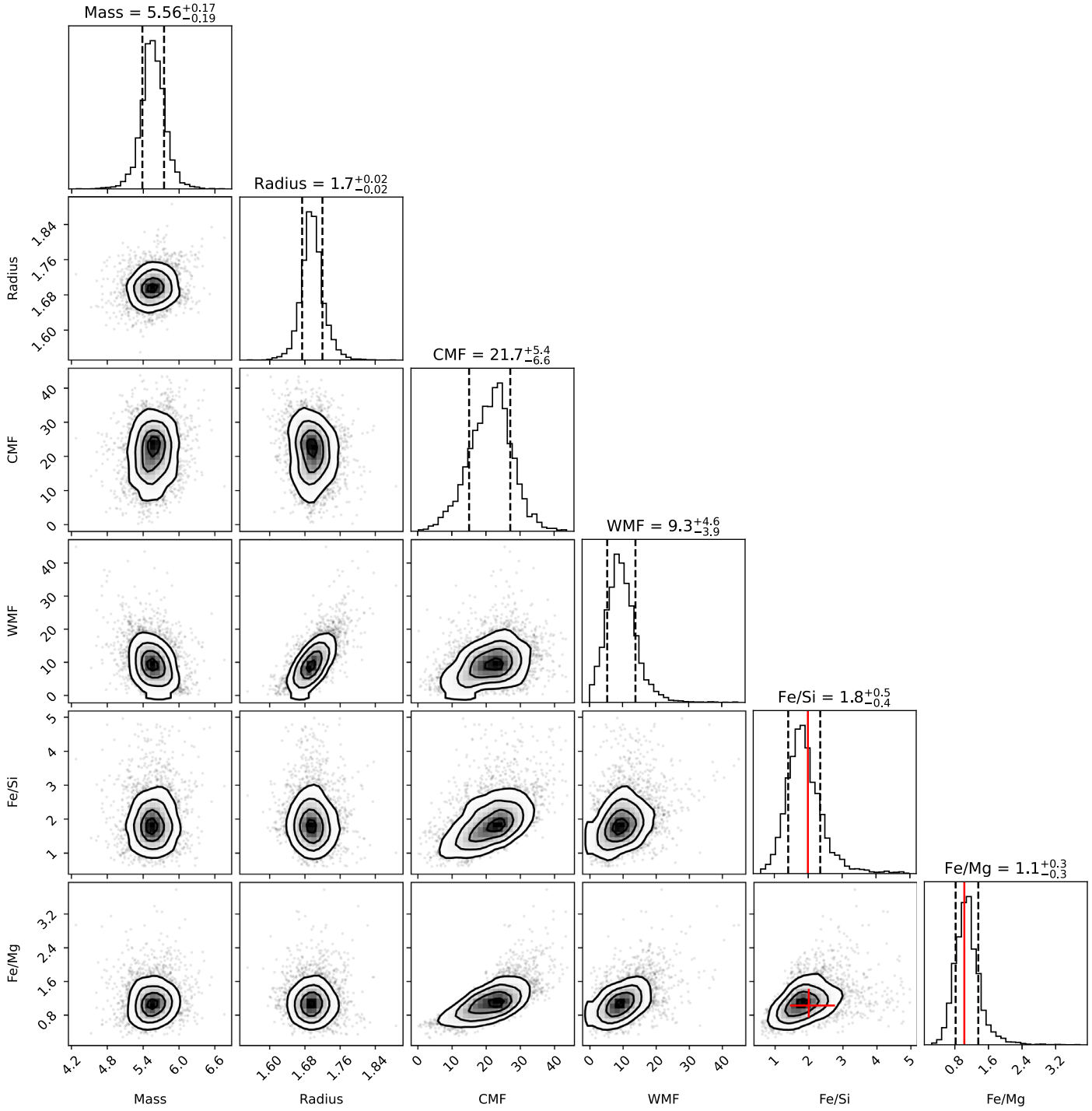

Figure E4. Posterior distribution for LHS 1140 b interior parameters for the Hycean world scenario (icy planet with 250 km H_2 atmosphere on top). Here, we use the same assumptions as the stellar prior water-world model. The red lines (and red cross) represent the stellar ratios, while the vertical black dashed lines are the 16th and 84th percentiles of the posterior. Note that the simulation radius is smaller ($\Delta R_p \sim 0.03\ R_\oplus$) due to the H_2 atmosphere, which is not included in our interior model.

ORCID iDs

Charles Cadieux https://orcid.org/0000-0001-9291-5555
Mykhaylo Plotnykov https://orcid.org/0000-0002-9479-2744
René Doyon https://orcid.org/0000-0001-5485-4675
Diana Valencia https://orcid.org/0000-0003-3993-4030
Farbod Jahandar https://orcid.org/0000-0003-0029-2835
Lisa Dang https://orcid.org/0000-0003-4987-6591
Martin Turbet https://orcid.org/0000-0003-2260-9856
Thomas J. Fauchez https://orcid.org/0000-0002-5967-9631
Ryan Cloutier https://orcid.org/0000-0001-5383-9393
Collin Cherubim https://orcid.org/0000-0002-8466-5469
Étienne Artigau https://orcid.org/0000-0003-3506-5667
Neil J. Cook https://orcid.org/0000-0003-4166-4121
Billy Edwards https://orcid.org/0000-0002-5494-3237
Tim Hallatt https://orcid.org/0000-0003-4992-8427
Benjamin Charnay https://orcid.org/0000-0003-0977-6545
François Bouchy https://orcid.org/0000-0002-7613-393X
Romain Allart https://orcid.org/0000-0002-1199-9759
Lucile Mignon https://orcid.org/0000-0002-5407-3905
Frédérique Baron https://orcid.org/0000-0002-5074-1128
Susana C. C. Barros https://orcid.org/0000-0003-2434-3625
Björn Benneke https://orcid.org/0000-0001-5578-1498
B. L. Canto Martins https://orcid.org/0000-0001-5578-7400
Nicolas B. Cowan https://orcid.org/0000-0001-6129-5699
J. R. De Medeiros https://orcid.org/0000-0001-8218-1586
Xavier Delfosse https://orcid.org/0000-0001-5099-7978
Elisa Delgado-Mena https://orcid.org/0000-0003-4434-2195
Xavier Dumusque https://orcid.org/0000-0002-9332-2011
David Ehrenreich https://orcid.org/0000-0001-9704-5405
Yolanda G. C. Frensch https://orcid.org/0000-0003-4009-0330
J. I. González Hernández https://orcid.org/0000-0002-0264-7356
Nathan C. Hara https://orcid.org/0000-0001-9232-3314
David Lafrenière https://orcid.org/0000-0002-6780-4252
Gaspare Lo Curto https://orcid.org/0000-0002-1158-9354
Lison Malo https://orcid.org/0000-0002-8786-8499
Claudio Melo https://orcid.org/0000-0002-6090-8446
Dany Mounzer https://orcid.org/0000-0002-8070-2058
Vera Maria Passeger https://orcid.org/0000-0002-8569-7243
Francesco Pepe https://orcid.org/0000-0002-9815-773X
Nuno C. Santos https://orcid.org/0000-0003-4422-2919
Alejandro Suárez Mascareño https://orcid.org/0000-0002-3814-5323
Simon Thibault https://orcid.org/0000-0002-2791-0595
Valentina Vaulato https://orcid.org/0000-0001-7329-3471
Gregg A. Wade https://orcid.org/0000-0002-1854-0131
François Wildi https://orcid.org/0000-0002-9216-4402

References

Adibekyan, V., Dorn, C., Sousa, S. G., et al. 2021, Sci, 374, 330
Agol, E., Dorn, C., Grimm, S. L., et al. 2021, PSJ, 2, 1
Aguichine, A., Mousis, O., Deleuil, M., & Marcq, E. 2021, ApJ, 914, 84
Ahumada, R., Prieto, C. A., Almeida, A., et al. 2020, ApJS, 249, 3
Akeson, R. L., Chen, X., Ciardi, D., et al. 2013, PASP, 125, 989
Albert, L., Lafrenière, D., Doyon, R., et al. 2023, PASP, 135, 075001
Allard, F., Homeier, D., & Freytag, B. 2012, RSPTA, 370, 2765
Allart, R., Lovis, C., Faria, J., et al. 2022, A&A, 666, A196
Ambikasaran, S., Foreman-Mackey, D., Greengard, L., Hogg, D. W., & O'Neil, M. 2015, ITPAM, 38, 252
Anglada-Escudé, G., Amado, P. J., Barnes, J., et al. 2016, Natur, 536, 437
Anglada-Escudé, G., & Butler, R. P. 2012, ApJS, 200, 15
Artigau, É., Cadieux, C., Cook, N. J., et al. 2022, AJ, 164, 84
Asplund, M., Amarsi, A. M., & Grevesse, N. 2021, A&A, 653, A141
Astropy Collaboration, Price-Whelan, A. M., Sipőcz, B. M., et al. 2018, AJ, 156, 123
Astudillo-Defru, N., Díaz, R. F., Bonfils, X., et al. 2017, A&A, 605, L11
Batalha, N. E., Mandell, A., Pontoppidan, K., et al. 2017, PASP, 129, 064501
Bell, T. J., Dang, L., Cowan, N. B., et al. 2021, MNRAS, 504, 3316
Benedict, G. F., Henry, T. J., Franz, O. G., et al. 2016, AJ, 152, 141
Benneke, B., & Seager, S. 2013, ApJ, 778, 153
Bensby, T., Feltzing, S., & Lundström, I. 2003, A&A, 410, 527
Bertaux, J. L., Lallement, R., Ferron, S., Boonne, C., & Bodichon, R. 2014, A&A, 564, A46
Binney, J., & Tremaine, S. 2008, Galactic Dynamics (2nd. ed.; Princeton, NJ: Princeton Univ. Press)
Blanco-Cuaresma, S. 2019, MNRAS, 486, 2075
Bland-Hawthorn, J., & Gerhard, O. 2016, ARA&A, 54, 529
Böker, T., Beck, T. L., Birkmann, S. M., et al. 2023, PASP, 135, 038001
Bond, J. C., O'Brien, D. P., & Lauretta, D. S. 2010, ApJ, 715, 1050
Bonsor, A., Jofré, P., Shorttle, O., et al. 2021, MNRAS, 503, 1877
Bouchy, F., Doyon, R., Artigau, É., et al. 2017, Msngr, 169, 21
Bouchy, F., Pepe, F., & Queloz, D. 2001, A&A, 374, 733
Boutle, I. A., Mayne, N. J., Drummond, B., et al. 2017, A&A, 601, A120
Cadieux, C., Doyon, R., Plotnykov, M., et al. 2022, AJ, 164, 96
Carter, P. J., Leinhardt, Z. M., Elliott, T., Walter, M. J., & Stewart, S. T. 2015, ApJ, 813, 72
Charnay, B., Blain, D., Bézard, B., et al. 2021, A&A, 646, A171
Charnay, B., Meadows, V., Misra, A., Leconte, J., & Arney, G. 2015, ApJL, 813, L1
Cherubim, C., Cloutier, R., Charbonneau, D., et al. 2023, AJ, 165, 167
Cloutier, R., Doyon, R., Bouchy, F., & Hébrard, G. 2018, AJ, 156, 82
Cloutier, R., & Menou, K. 2020, AJ, 159, 211
Cook, N. J., Artigau, É., Doyon, R., et al. 2022, PASP, 134, 114509
Coulombe, L.-P., Benneke, B., Challener, R., et al. 2023, Natur, 620, 292
Dang, L., Cowan, N. B., Schwartz, J. C., et al. 2018, NatAs, 2, 220
Dawson, R. I., & Johnson, J. A. 2012, ApJ, 756, 122
Del Genio, A. D., Brain, D., Noack, L., & Schaefer, L. 2020, Planetary Astrobiology (Tucson, AZ: Univ. Arizona Press), 419
Del Genio, A. D., Way, M. J., Amundsen, D. S., et al. 2019, AsBio, 19, 99
Delmotte, N., Dolensky, M., Padovani, P., et al. 2006, in ASP Conf. Ser. 351, Astronomical Data Analysis Software and Systems XV, ed. C. Gabriel et al. (San Francisco, CA: ASP), 690
Deming, D., Knutson, H., Kammer, J., et al. 2015, ApJ, 805, 132
Diamond-Lowe, H., Berta-Thompson, Z., Charbonneau, D., Dittmann, J., & Kempton, E. M. R. 2020, AJ, 160, 27
Dittmann, J. A., Irwin, J. M., Charbonneau, D., et al. 2017, Natur, 544, 333
Donati, J. F., Kouach, D., Moutou, C., et al. 2020, MNRAS, 498, 5684
Dorn, C., Hinkel, N. R., & Venturini, J. 2017, A&A, 597, A38
Doyon, R., Willott, C. J., Hutchings, J. B., et al. 2023, PASP, 135, 098001
Dumusque, X. 2018, A&A, 620, A47
Edwards, B., Changeat, Q., Mori, M., et al. 2021, AJ, 161, 44
Espinoza, N. 2018, RNAAS, 2, 209
Espinoza, N., Kossakowski, D., & Brahm, R. 2019, MNRAS, 490, 2262
Faria, J. P., Suárez Mascareño, A., Figueira, P., et al. 2022, A&A, 658, A115
Fauchez, T. J., Turbet, M., Villanueva, G. L., et al. 2019, ApJ, 887, 194
Fazio, G. G., Hora, J. L., Allen, L. E., et al. 2004, ApJS, 154, 10
Foreman-Mackey, D. 2016, JOSS, 1, 24
Foreman-Mackey, D., Hogg, D. W., Lang, D., & Goodman, J. 2013, PASP, 125, 306
Forget, F., & Leconte, J. 2014, RSPTA, 372, 20130084
Fulton, B. J., Petigura, E. A., Blunt, S., & Sinukoff, E. 2018, PASP, 130, 044504
Fulton, B. J., Petigura, E. A., Howard, A. W., et al. 2017, AJ, 154, 109
Gaia Collaboration, Brown, A. G. A., Vallenari, A., et al. 2021, A&A, 649, A1
Gaia Collaboration, Vallenari, A., Brown, A. G. A., et al. 2023, A&A, 674, A1
Gan, T., Cadieux, C., Jahandar, F., et al. 2023, AJ, 166, 165
Gardner, J. P., Mather, J. C., Abbott, R., et al. 2023, PASP, 135, 068001
Gillon, M., Triaud, A. H. M. J., Demory, B.-O., et al. 2017, Natur, 542, 456
Ginzburg, S., Schlichting, H. E., & Sari, R. 2016, ApJ, 825, 29
Ginzburg, S., Schlichting, H. E., & Sari, R. 2018, MNRAS, 476, 759
Guillot, T., & Morel, P. 1995, A&AS, 109, 109
Hallatt, T., & Wiegert, P. 2020, AJ, 159, 147
Harris, C. R., Millman, K. J., van der Walt, S. J., et al. 2020, Natur, 585, 357

Hawkins, K., Jofré, P., Masseron, T., & Gilmore, G. 2015, MNRAS, 453, 758
Haywood, R. D., Collier Cameron, A., Queloz, D., et al. 2014, MNRAS, 443, 2517
Hemley, R. J., Jephcoat, A. P., Mao, H. K., et al. 1987, Natur, 330, 737
Higson, E., Handley, W., Hobson, M., & Lasenby, A. 2019, S&C, 29, 891
Hunter, J. D. 2007, CSE, 9, 90
Husser, T. O., Wende-von Berg, S., Dreizler, S., et al. 2013, A&A, 553, A6
Inamdar, N. K., & Schlichting, H. E. 2016, ApJL, 817, L13
Irwin, J., Charbonneau, D., Nutzman, P., & Falco, E. 2009, in IAU Symp. 253, Transiting Planets (Cambridge: Cambridge Univ. Press), 37
Jahandar, F., Doyon, R., Artigau, É., et al. 2023, arXiv:2310.12125
Jenkins, J. M., Twicken, J. D., McCauliff, S., et al. 2016, Proc. SPIE, 9913, 99133E
Karamanis, M., Beutler, F., & Peacock, J. A. 2021, MNRAS, 508, 3589
Kipping, D. M. 2010, MNRAS, 407, 301
Kipping, D. M. 2013, MNRAS, 435, 2152
Kipping, D. M. 2014, MNRAS, 440, 2164
Kite, E. S., & Ford, E. B. 2018, ApJ, 864, 75
Kordopatis, G., Schultheis, M., McMillan, P. J., et al. 2023, A&A, 669, A104
Kreidberg, L. 2015, PASP, 127, 1161
Leconte, J., Wu, H., Menou, K., & Murray, N. 2015, Sci, 347, 632
Lee, E. J., & Connors, N. J. 2021, ApJ, 908, 32
Li, C., & Zhao, G. 2017, ApJ, 850, 25
Lillo-Box, J., Figueira, P., Leleu, A., et al. 2020, A&A, 642, A121
Lindegren, L., Klioner, S. A., Hernández, J., et al. 2021, A&A, 649, A2
Luque, R., & Pallé, E. 2022, Sci, 377, 1211
Madhusudhan, N., Piette, A. A. A., & Constantinou, S. 2021, ApJ, 918, 1
Madhusudhan, N., Sarkar, S., Constantinou, S., et al. 2023, ApJL, 956, L13
Majewski, S. R. & APOGEE Team 2016, AN, 337, 863
Mann, A. W., Dupuy, T., Kraus, A. L., et al. 2019, ApJ, 871, 63
Mann, A. W., Feiden, G. A., Gaidos, E., Boyajian, T., & von Braun, K. 2015, ApJ, 804, 64
Marounina, N., & Rogers, L. A. 2020, ApJ, 890, 107
Ment, K., Dittmann, J. A., Astudillo-Defru, N., et al. 2019, AJ, 157, 32
Morrison, R. A., Jackson, J. M., Sturhahn, W., Zhang, D., & Greenberg, E. 2018, JGRB, 123, 4647
Owen, J. E., & Wu, Y. 2017, ApJ, 847, 29
Patel, J. A., & Espinoza, N. 2022, AJ, 163, 228
Pepe, F., Cristiani, S., Rebolo, R., et al. 2021, A&A, 645, A96
Pepe, F., Mayor, M., Rupprecht, G., et al. 2002, Msngr, 110, 9
Piaulet, C., Benneke, B., Almenara, J. M., et al. 2023, NatAs, 7, 206
Plotnykov, A., & Valencia, D. 2020, MNRAS, 499, 932
Rajpaul, V., Aigrain, S., Osborne, M. A., Reece, S., & Roberts, S. 2015, MNRAS, 452, 2269
Reddy, B. E., Lambert, D. L., & Allende Prieto, C. 2006, MNRAS, 367, 1329
Reylé, C., Jardine, K., Fouqué, P., et al. 2021, A&A, 650, A201
Reylé, C., Jardine, K., Fouqué, P., et al. 2022, in The 21st Cambridge Workshop on Cool Stars, Stellar Systems, and the Sun, ed. A. S. Brun, J. Bouvier, & P. Petit, 218
Ribas, I., Bolmont, E., Selsis, F., et al. 2016, A&A, 596, A111
Ricker, G. R., Winn, J. N., Vanderspek, R., et al. 2015, JATIS, 1, 014003
Rogers, J. G., Schlichting, H. E., & Owen, J. E. 2023, ApJL, 947, L19
Rogers, L. A. 2015, ApJ, 801, 41
Sabotta, S., Schlecker, M., Chaturvedi, P., et al. 2021, A&A, 653, A114
Scora, J., Valencia, D., Morbidelli, A., & Jacobson, S. 2020, MNRAS, 493, 4910
Seager, S., & Mallén-Ornelas, G. 2003, ApJ, 585, 1038
Silva, A. M., Faria, J. P., Santos, N. C., et al. 2022, A&A, 663, A143
Skrutskie, M. F., Cutri, R. M., Stiening, R., et al. 2006, AJ, 131, 1163
Smith, J. C., Stumpe, M. C., Van Cleve, J. E., et al. 2012, PASP, 124, 1000
Spaargaren, R. J., Wang, H. S., Mojzsis, S. J., Ballmer, M. D., & Tackley, P. J. 2023, ApJ, 948, 53
Speagle, J. S. 2020, MNRAS, 493, 3132
Stewart, S. T., & Ahrens, T. J. 2005, JGRE, 110, E03005
Stixrude, L., & Lithgow-Bertelloni, C. 2011, GeoJI, 184, 1180
Stock, S., Kemmer, J., Kossakowski, D., et al. 2023, A&A, 674, A108
Stumpe, M. C., Smith, J. C., Catanzarite, J. H., et al. 2014, PASP, 126, 100
Stumpe, M. C., Smith, J. C., Van Cleve, J. E., et al. 2012, PASP, 124, 985
Suárez Mascareño, A., González-Álvarez, E., Zapatero Osorio, M. R., et al. 2023, A&A, 670, A5
Thiabaud, A., Marboeuf, U., Alibert, Y., Leya, I., & Mezger, K. 2015, A&A, 580, A30
Trotta, R. 2008, ConPh, 49, 71
Tsiaras, A., Waldmann, I. P., Rocchetto, M., et al. 2016, ApJ, 832, 202
Turbet, M., Bolmont, E., Ehrenreich, D., et al. 2020, A&A, 638, A41
Turbet, M., Bolmont, E., Leconte, J., et al. 2018, A&A, 612, A86
Turbet, M., Fauchez, T. J., Leconte, J., et al. 2023, A&A, 679, A126
Turbet, M., Leconte, J., Selsis, F., et al. 2016, A&A, 596, A112
Unterborn, C. T., Dismukes, E. E., & Panero, W. R. 2016, ApJ, 819, 32
Valencia, D., Guillot, T., Parmentier, V., & Freedman, R. S. 2013, ApJ, 775, 10
Valencia, D., Sasselov, D. D., & O'Connell, R. J. 2007, ApJ, 656, 545
Van Eylen, V., & Albrecht, S. 2015, ApJ, 808, 126
Villanueva, G. L., Liuzzi, G., Faggi, S., et al. 2022, Fundamentals of the Planetary Spectrum Generator (Greenbelt, MD: Library of Congress)
Villanueva, G. L., Smith, M. D., Protopapa, S., Faggi, S., & Mandell, A. M. 2018, JQSRT, 217, 86
Virtanen, P., Gommers, R., Oliphant, T. E., et al. 2020, NatMe, 17, 261
Wagner, W., & Pruß, A. 2002, JPCRD, 31, 387
Waskom, M. 2021, JOSS, 6, 3021
Wildi, F., Bouchy, F., Doyon, R., et al. 2022, Proc. SPIE, 12184, 121841H
Wolf, E. T., Shields, A. L., Kopparapu, R. K., Haqq-Misra, J., & Toon, O. B. 2017, ApJ, 837, 107
Wordsworth, R. D., Forget, F., Selsis, F., et al. 2011, ApJL, 733, L48
Yang, J., Ji, W., & Zeng, Y. 2020, NatAs, 4, 58
Zechmeister, M., Reiners, A., Amado, P. J., et al. 2018, A&A, 609, A12